

Ultra fast MRI acquisition at 7 Tesla

Implementation of Wave-CAIPI with a high
efficiency head insert gradient coil

by

A. Monreal Madrigal

to obtain the degree of Master of Science
at the Delft University of Technology,
to be defended publicly on Thursday September 09, 2020 at 03:00 PM.

Student number: 4833074
Project duration: January 1, 2020 – September 09, 2020
Thesis committee: Dr. ir. R.F. Remis, TU Delft, supervisor
Dr. N. Budko, TU Delft
Dr. ir. J.C.W. Siero UMC, Utrecht
ir. E. Versteeg UMC, Utrecht



An electronic version of this thesis is available at <http://repository.tudelft.nl/>.

CONTENTS

1	Introduction	5
1.1	Magnetic Resonance Imaging	6
1.1.1	Hardware	9
1.1.2	Signal generation and detection	9
1.1.3	K-space	12
1.1.4	Image reconstruction	13
1.1.5	Parallel Imaging	14
2	Head insert gradient Coil	17
3	Wave-CAIPI	19
3.1	2D CAIPIRINHA and Bunched Phased Encoding	19
3.2	Wave-CAIPI	20
3.3	Image reconstruction	22
3.4	Quality assessment	23
4	Methods	25
4.1	Simulations	25
4.1.1	Wave-CAIPI method simulation	25
4.1.2	Quality assessment	33
4.2	Parameters optimization	33
4.2.1	Range of spread effect	34
4.2.2	Number of sine cycles effect	35
4.2.3	Pixel Bandwidth effect	35
4.2.4	Time gain, conventional gradient vs insert gradient	36
4.3	Implementation in scanner	37
4.3.1	Imaging experiments and reconstruction	38
5	Results	43
5.1	Simulations	43
5.2	Parameters optimization	45
5.2.1	Range of spread effect	45
5.2.2	Number of sine cycles effect	47
5.2.3	Pixel Bandwidth effect	50
5.2.4	Time gain, conventional gradient vs insert gradient	53
5.3	Implementation in scanner	56
5.3.1	Imaging experiments and reconstruction	56

6	Discussion, conclusions, limitations and further work	61
6.1	Limitations	62
6.2	Further work	63
	Bibliography	64

ACKNOWLEDGEMENTS

I want to thank my thesis advisers from the UMC Utrecht, Dr. Jeroen Siero, and ir. Edwin Versteeg to give me the opportunity and guide me during this exciting project. Special thanks to Edwin for being available to answer any question and have hours-long meetings at any time, even when working from home. I would also like to thank my TU Delft supervisor, Dr. Rob Remis, for giving me important feedback and helping with the project's planning to make sure I delivered everything on time. In no lesser extent, I would like to thank Dr. Neil Budko for agreeing to be part of my thesis committee.

To my parents and brothers who always supported me and helped make it possible to obtain my master's degree from TU Delft; to my loved ones that passed away during these two years. I would also like to thank Mexico's government that financially supported my master's degree.

ABSTRACT

Magnetic Resonance Imaging is one of the most widely used imaging modalities nowadays and it performs especially well imaging human organs such as the brain and liver. One of its main limitations is the relatively long imaging times, to overcome this issue and speed up the data acquisition, several techniques such as Parallel Imaging or PI have been developed. These techniques require advanced hardware and software to be able to decrease the acquisition time. On the hardware side, a highly efficient insert gradient coil has been designed and built at the University Medical Center Utrecht. Specialized software has to be implemented to optimally make use of this hardware. One of the recently proposed PI methods called Wave-CAIPI has been proved to achieve a ninth fold acceleration factor without compromising image quality.

This project aims to investigate the time gain that can be achieved when combining the insert gradient coil with a Wave-CAIPI strategy. Two main aspects are reviewed. The first one is the maximum achievable under-sampling factor that does not compromise image quality. The second one is the decrease in acquisition time that can be obtained when using the insert gradient coil compared to conventional gradient systems while maintaining image quality. To do so, the strategy has been implemented and extensive simulations have been performed to optimize the MR acquisition parameters. To prove the results from the simulations, the Wave-CAIPI sequence was implemented in a 7T scanner at the UMCU, where the acquired data was retrospectively under-sampled, obtaining the wave image to be further reconstructed.

Limitations of previous works on Wave-CAIPI have been the gradient specifications, which can be overcome by the high-efficiency coil. It has been concluded that shorter acquisition times without compromising image quality are possible when using the insert coil compared with conventional systems. The time gain can be up to a factor of five, and sixteen fold under-sampling factors could be possible. The time gain can be especially useful for Echo Planar Imaging sequences, where switching faster gradients allows to acquire more signals in less time. The next steps for this research are to prospectively under-sample the data in a Wave-CAIPI fashion with a sixteen under-sampling factor and corroborate if sequences such as Echo Planar Imaging can be benefited with the time gain.

1

INTRODUCTION

Nuclear Magnetic Resonance Imaging, also known as Magnetic Resonance Imaging or MRI, is currently one of the most popular medical imaging modalities worldwide. Up until the mid-70s, the most advanced, efficient, and safe medical imaging technology was Computer Tomography or CT, which uses X-rays and advanced image reconstruction techniques to generate a cross-sectional image of a specific section or organ of a patient. One of the main drawbacks of CT is that during the image acquisition, the patient is exposed to radiation. Therefore, MRI has come along as a preferred technology since it does not use radiation to generate an image of a patient's body.

MRI has many advantages as it can generate images at millimeter resolution and performs especially well when imaging soft human tissues such as the brain, liver and other major organs. Nevertheless, two of its main limitations are the cost of the scanner, which can be as triple as a CT and the relatively long imaging times. A typical clinical imaging protocol takes on average 20-60 minutes [1], this is particularly a problem since the patient has to stay still during the signal acquisition, patient movements can cause artifacts in the final image. For this reason, a hot topic in MRI research focuses on developing different methods and techniques that can significantly shorten the imaging time using state of the art hardware and algorithms.

This work investigates the time gain that can be achieved when combining a highly efficient head gradient coil [2] with a recently proposed parallel imaging technique called Wave-CAIPI [3] at a 7 Tesla scanner. This time gain was explored in a simulation study which includes an optimization of acquisition and reconstruction parameters. The highest feasible acceleration factor that does not compromise image quality is investigated, a comparison of the imaging times using the conventional and insert gradient is also provided. Additionally, the Wave-CAIPI sequence was implemented on a 7T MR-scanner and the quality of the reconstructed images, was validated against simulations and literature.

This report's structure is as follows: the following section briefly describes the principles of MRI; its hardware, how signals are generated, and the image reconstruction process; the concepts introduced there allow to describe advanced MRI techniques in the

following chapters. Chapter 2 introduces the main characteristics of the head insert gradient coil presented in [4], this coil allows the gradient in the z-direction to be switched on and off at a higher rate, being capable of reducing signal acquisition time. Chapter 3 describes the Wave-CAIPI method presented in [3]; it presents a brief introduction and its mathematical formulation, this parallel imaging technique allows a significant imaging time reduction without compromising image quality. Chapters 4 and 5 describe the methods and results of this project. Lastly, chapter 6 presents the discussion, conclusions, and further work.

1.1. MAGNETIC RESONANCE IMAGING

MRI is a medical imaging modality that takes advantage of the magnetic moment generated by the spin of certain nuclei to generate high-resolution, high-contrast, cross-sectional images of the anatomy and physiological processes of the human body. The signals used to create the image arise from the nuclear magnetic resonance properties of some nuclei, which can be stimulated in various forms when placed inside a fixed magnetic field with the help of variable Radio Frequency fields. The subject's part of the body to be imaged is virtually divided into different volumetric sections called voxels, which are in the order of squared millimeters. To generate the final image, a gray-scale value that depends on the intensity of the signal generated by the spins present in each voxel is assigned to each of these units.

Nuclear Magnetic Resonance NMR is the physical phenomenon used in MRI to generate an image. It is well known that nuclei present a positive charge since it is composed of protons and neutrons. Some of these nuclei, the ones with odd atomic or mass number, present charge, and angular momentum. This type of nuclei are said to have spin. From Maxwell's equations, it is known that circulating charges generate a magnetic field, which in turn creates an electric field; the combination of these two produces an electromagnetic field. The nuclei that spins also possess a microscopic magnetic field, a typical presentation of the spin of nuclei is of a positive charge spinning around its axis as in figure 1.1a. The magnetic moment vector μ of this microscopic magnetic field is described by equation 1.1, where γ is the gyromagnetic ratio and Φ the angular momentum.

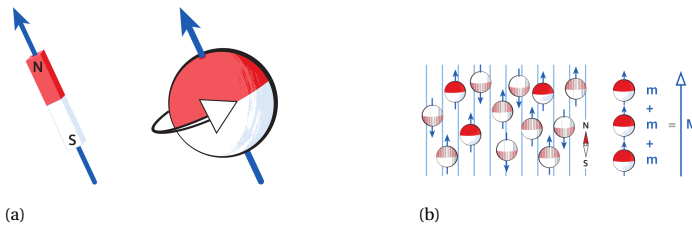


Figure 1.1: Visual representation of spins, 1.1a typical representation of the spin of a nuclei and 1.1b vector representation of sum of spins, reprinted from [5]

$$\mu = \gamma \Phi \quad (1.1)$$

In normal conditions, these individual nuclear spins have random orientation and cancel each other. Nevertheless, when placed into an external magnetic field B_0 of higher amplitude they tend to align with it. When aligning, their combined effect produce a *spin system* which is a collection of individual spins that can be modeled using a bulk magnetization vector \mathbf{M} , this vector is said to become magnetized when placed in an external magnetic field as shown in figure 1.1b. If the spin system does not get disturbed, it will reach equilibrium when placed into the static magnetic field and it will be parallel to B_0 . The magnitude of this vector is described by equation 1.3, where $k = 1.38 \times 10^{-23} J \cdot K^{-1}$ is Boltzmann's constant, $h = 6.26 \times 10^{-34} J \cdot s$ is Planck's constant, T is temperature in degrees Kelvin and P_D is the proton density or the number of nuclei per unit volume. It is important to note that the $\mathbf{M}(\mathbf{r}, t)$ is a function of position in the 3D space and time, for visual representation the position dependency \mathbf{r} is dropped from the notation.

$$\mathbf{M}(t) = \sum_{n=1}^{N_s} \mu_n \quad (1.2)$$

$$M_0 = \frac{B_0 \frac{\gamma}{2\pi}^2 h^2}{4kT} P_D \quad (1.3)$$

The magnetization vector $\mathbf{M}(t)$ can be disturbed if different magnetic fields are applied. These time-variant magnetic fields capable of modifying the magnetization vectors are realized turning on and off different gradient coils and generating Radio Frequency pulses. This time varying fields disturb the magnetic field and in turn the precessing frequency of $\mathbf{M}(t)$ is modified as a function of space and time. Since $\mathbf{M}(t)$ is a magnetic moment, it experiences a torque if a time-varying magnetic field $\mathbf{B}(t)$ is applied, this is described by:

$$\frac{d\mathbf{M}(t)}{dt} = \gamma \mathbf{M}(t) \times \mathbf{B}(t) \quad (1.4)$$

One of the fundamental equations of MRI is the so-called Larmor frequency, equation 1.5, which describes the rate of precession of the magnetic moment around the external magnetic field, and it has units of radians per second. A visual representation of the precession phenomenon can be found in figure 1.2a.

$$\omega_0 = \gamma B_0 \quad (1.5)$$

The vector $\mathbf{M}(t)$ can be divided into its *longitudinal* M_z and *transverse* M_{xy} components in the complex plane as seen in figure 1.2b. In MRI, the longitudinal component points to the same direction as the static field, whereas the transverse is oriented orthogonal to the main field, equations 1.6 and 1.7 represent the decomposition of $\mathbf{M}(t)$. The angle between the components of $\mathbf{M}(t)$ is characterized by equation 1.8 and is called phase of the transverse magnetization.

$$M_z(t) = M_z(t) \quad (1.6)$$

$$M_{xy}(t) = M_x(t) + jM_y(t) \quad (1.7)$$

$$\phi = \tan^{-1} \frac{M_y}{M_x} \quad (1.8)$$

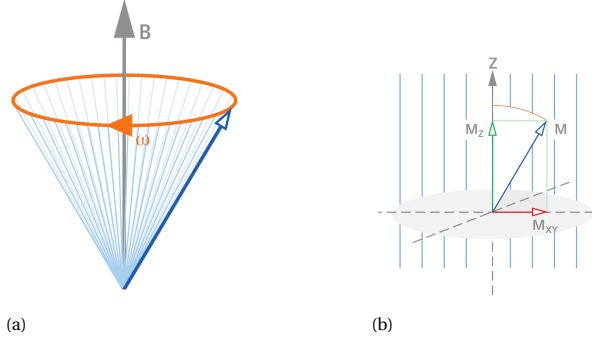


Figure 1.2: Visual representation of precession phenomenon, 1.2a Vector $\mathbf{M}(t)$ precessing and 1.2b its longitudinal M_z and transverse M_{xy} components [5]

From Faraday's law of induction, we know that a time-varying magnetic field cutting across a coil of wire will induce a voltage. Using this principle, receiver RF coils are placed close to the area to be imaged; the transverse magnetization will generate a voltage in the receiver coil. The voltage generated in the coil represents the *signal* and is given by:

$$V(t) = -\frac{\partial}{\partial t} \int_{object} \mathbf{M}(\mathbf{r}, t) \cdot \mathbf{B}^r(\mathbf{r}) d\mathbf{r} \quad (1.9)$$

Where \mathbf{r} is the vector of position in the 3D plane $\mathbf{r} = (x, y, z)$ and \mathbf{B} represents the magnetic field.

Applying a RF pulse is possible to move the spin system out of equilibrium. To do so, the new time-varying RF field B_1 has to match the Larmor frequency, equation 1.5 of the magnetization vector, this will push the vector towards the transverse plane. Using a circular polarized RF excitation with a rectangular envelope $B_1^e(t)$, the RF field is given by equation 1.10. The final tip angle α and phase ϕ of \mathbf{M} depends on the amplitude and duration of $B_1^e(t)$.

$$B_1(t) = B_1^e(t) e^{j\phi} \quad (1.10)$$

$$\alpha = \gamma \int_0^{\tau_p} B_1^e(t) dt \quad (1.11)$$

Once the magnetization is flipped with an angle α , $\mathbf{M}(t)$ will precess and two relaxation processes will occur, *longitudinal* and *transverse* relaxation. The first one describes the recovery of the longitudinal magnetization M_z , which gets back to its equilibrium, this happens in an exponential fashion and its characterized by the so called longitudinal relaxation time T_1 . On the other hand, the *transverse* relaxation refers to the exponential decay of M_{xy} and its time constant T_2 describes the transverse relaxation time. T_1 and T_2 times are tissue specific and are important mechanisms to generate contrast in the final image.

Another important equation in MRI is the Bloch equation, which describes the behavior of the magnetization $\mathbf{M}(t)$ for a given magnetic field B with respect to a reference frame rotating at Larmor frequency. This equation is used to model how the magnetization vector behaves during and after an excitation pulse. The Bloch equation for the general case is:

$$\frac{\partial \mathbf{M}(\mathbf{r}, t)}{\partial t} + \gamma \mathbf{B}(\mathbf{r}, t) \times \mathbf{M}(\mathbf{r}, t) + \frac{1}{T_2(\mathbf{r})} M_{xy}(\mathbf{r}, t) + \frac{1}{T_1(\mathbf{r})} M_z(\mathbf{r}, t) = \frac{1}{T_1(\mathbf{r})} M^{eq}(\mathbf{r}) \mathbf{i}_z \quad (1.12)$$

1.1.1.1. HARDWARE

Different components of the MRI scanner work together to make the physical phenomenon described above take place. The main five components of an MRI system are: *main magnet*, in most of the clinical scanners its magnitude is >1 T and is responsible for the alignment of spins. *Gradient coils*, which are turned on and off during the image acquisition to provide spatial localization of the signal. *RF coils*, which transmit and receive radio frequency pulses and signals; these coils are capable of flipping the magnetization to the transverse plane. *Electronics* to program the timing for the transmission and reception of signals. *Console* to view, manipulate and store the generated images. Figure 1.3 presents a block diagram and the different components of an MRI system.

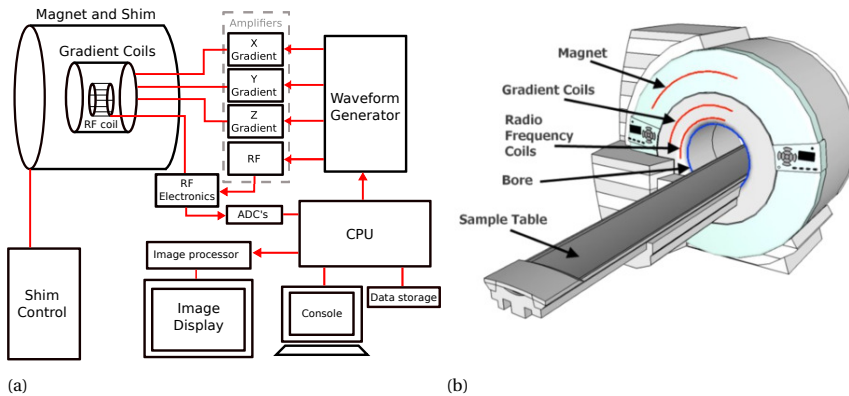


Figure 1.3: Principal components of MRI system, 1.3a scanner electronics diagram and 1.3b scanner components, reprinted from [6]

1.1.2. SIGNAL GENERATION AND DETECTION

When the magnetization vector is flipped along the transverse plane, an MR signal is generated, two of the principal mechanisms to generate this signal are *spin echo* and *gradient echo*, the principle underlying this signal generation is to make spins precess with the same phase, so the magnitude of magnetization vector is as large as possible. Spin echo consists of a 90 degrees RF pulse to flip the magnetization, followed by a 180 degrees pulse that causes the spin to get in phase after some echo time TE. On the other hand, gradient echo switches negative gradients, followed by a positive one; this way, the

spins get in phase, and a larger signal is generated after some echo time TE, an example of pulse sequences of this type can be found in figure 1.5.

The signal generated is picked up by the Receiver RF coil, this signal corresponds to the magnetization vectors of all the excited area (flipped spins), for this reason, it is necessary to perform signal encoding to define the spatial location of each magnetization vector. Signal encoding is achieved by slightly modifying the Larmor frequencies as a function of position in the three dimensional space. *Slice selection*, *frequency encoding* and *phase encoding* are the steps followed to be able to determine where the signal is coming from and generate an image. These steps use the gradient coil system to modify the magnetic field's magnitude inside the scanner, which, as it can be seen from equation 1.5, will make spins precess at different frequencies depending on their spatial location. Figure 1.4 presents the visual intuition of this concept.

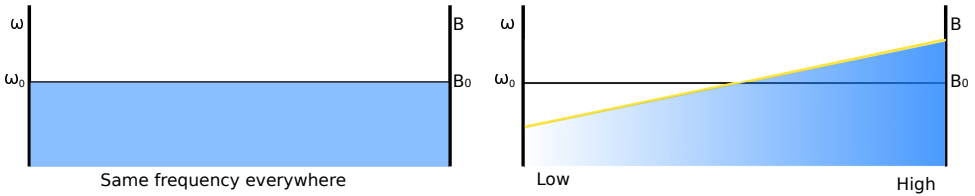


Figure 1.4: Visual representation of the effect of gradients in the Larmor frequency. Left: when the gradient is off, the B field and Larmor frequency ω is the same everywhere. Right: when the gradient is on, they depend on its spatial position

To select a specific slice, a *slice selection* gradient G_z is turned on at the same time as the RF transmit pulse. The gradient will modify the magnetic field amplitude and spins will precess at different frequencies. As stated before, to flip the magnetization to the transverse plane, a RF pulse with the same frequency as the spins to be flipped has to be applied. For this reason, the RF pulse consists of a waveform that excites a range of frequencies; this range is selected depending on the desired position and thickness of the slice. After the described steps are performed, only spins from a specific slice will be flipped to the transverse plane. In this work, the slice selection gradient is in the z -direction. The Larmor frequencies during a slice selection gradient are given by:

$$\omega(z) = \gamma(B_0 + G_z z) \quad (1.13)$$

Frequency encoding is the process used to define the location of spins in the readout direction, the same principle as slice selection is used; when a gradient G_x is applied, spins precess at different frequencies depending on their spatial location. This gradient is applied at the same time as the Analog to Digital Converter ADC. This process gives the spatial location in a second dimension. The frequencies along the readout direction, when this is in the x -direction are given by:

$$\omega(x) = \gamma(B_0 + G_x x) \quad (1.14)$$

To encode the signal in the third dimension, a process called *phase encoding* is used, as both slice and frequency encoding, it consists of turning on a gradient G_y for a specific time T_p , the spins will as well process with different frequencies along the gradient

direction and will accumulate phase, this phase accumulated is given by equation 1.15. The phase encoding gradient has to be turned on before the frequency encoding and after the slice selection gradient, if this dimension is y, the phase is given by:

$$\phi_y(y) = -\gamma G_y T_p y \quad (1.15)$$

Finally, the base-band signal acquired by the RF coil, which includes the effects of the three space encoding steps described above, is given by:

$$s_0(t) = \int_{-\infty}^{\infty} \int_{-\infty}^{\infty} f(x, y) e^{-j2\pi\gamma G_x x t} e^{-j2\pi\gamma G_y T_p y} dx dy \quad (1.16)$$

The steps described above have to be repeated several times until the desired field of view is covered. Three important parameters for the acquisitions are, Echo Time **TE**, Repetition Time **TR** and flip angle α , TE is the time it takes for an echo (peak signal intensity) to be generated, TR is the time between RF pulses applied to generate an echo and flip angle defines parameters for the RF pulse, these parameters are usually selected to generate a specific image contrast. This process can be visually represented in "pulse sequence diagrams," which are timelines of the events occurring during an MR scan; they represent the sequence on how the RF pulses, gradient coils, and ADC are activated for the signal generation and acquisition. Examples of this pulse sequence diagrams can be found in figure 1.5.

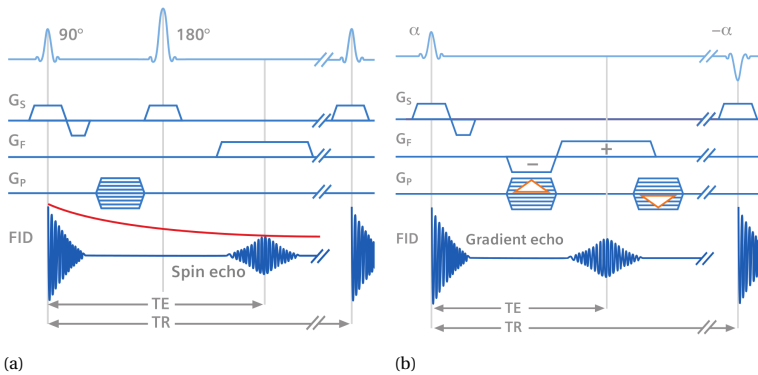


Figure 1.5: Pulse sequence diagrams for the two main mechanisms to generate MRI signal, 1.5a Spin Echo and 1.5b Gradient Echo, reprinted from [6]

The total scan time depends on the number of phase encoding steps PE_{steps} , TR and number of average signals NEX (acquisition of several signals with same parameters to average them and reduce noise) and can be calculated as:

$$T_{acquisition} = TR \times PE_{steps} \times NEX \quad (1.17)$$

The quality of a MRI image can be assessed by different factors, such as image resolution, Signal to Noise Ratio SNR and Artifacts present in the image. Image resolution is the level of detail of the image and is measured by the pixel size, SNR defines the ratio

between the actual signal and background noise, the SNR can be obtained with equation 1.18, artifacts are distortions in the image which can be generated by the type of sequence, fat or fluid signal, anatomy outside the Field of View FOV or presence of metallic objects.

$$SNR = \frac{|V|}{\sqrt{\sigma^2}} \quad (1.18)$$

Where $|V|$ and is the magnitude of the received signal and σ^2 is the variance of the received noise.

1.1.3. K-SPACE

MR systems acquire the signal in the frequency domain, which in MRI is called the **K-Space**. As mentioned before, turning the slice selection, frequency encoding and phase encoding gradients, slightly modifies the magnetic field, this make the spins precess at different frequencies and phases as a function of its spatial location. The K-space can be interpreted as a grid of points, each of them representing a sampling point of the different signals acquired, and as explained before, each point represents a different frequency.

Recording multiple signals to cover the whole area of interest is sometimes referred as filling the K-space. Two important parameters of this frequency domain grid are the distance between sampling points Δk and the point farther from the center of the k-space k_{max} , these two parameters represent the rate of sampling and the highest frequency acquired respectively. They are related to the user-selected parameters Field of View and pixel resolution Δ_w in the image domain. Their relation is given by:

$$\Delta k = 1/FOV \quad (1.19)$$

$$\Delta w = 1/k_{FOV} \quad (1.20)$$

$$K_{fov} = 2k_{max} \quad (1.21)$$

Equation 1.19 defines the minimum distance Δk between sampling points needed to reconstruct the image without artifacts with the desired FOV and is derived from the Nyquist-Shannon theorem [7], stating that to fully reconstruct a signal, it should be sampled at least twice the higher frequency.

As can be seen from equation 1.19, increasing the distance between K-space points Δk will reduce the FOV, and since the Nyquist-Shannon theorem is violated, artifacts will appear in the image domain. From equation 1.20, it can be seen that if we keep Δk constant, but reduce K_{fov} , the image domain will have the same FOV, but Δ_w will be increased so that the final image will have lower resolution. The effects of changing this parameters can be seen in figure 1.6.

An important characteristic of the K-space is that the center points are the ones with higher amplitude and represent the lower frequencies, whereas the points far from the center have lower amplitude and represent higher frequencies. When going from frequency to image domain, the center points form the shapes and basic contrast of the image, on the other hand, the points in the periphery give rise to the edges and details in the final image. This is in-line with the previously described spatial location strategy

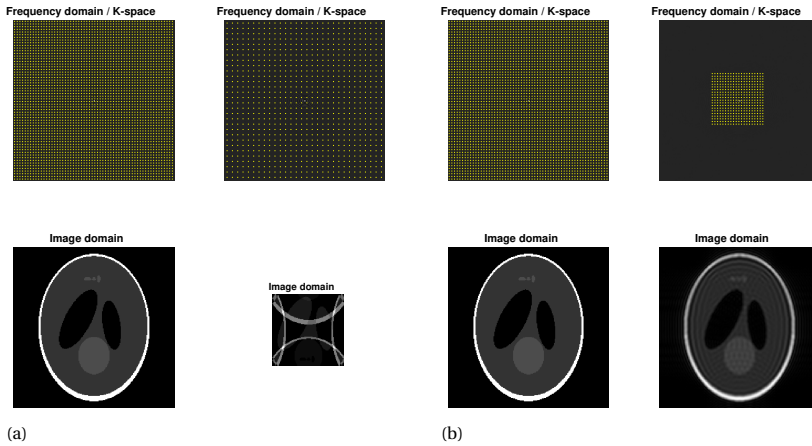


Figure 1.6: Effect of Δk in reconstructed image, **1.6a** doubling Δk and keeping k_{max} the same, produces an image of half the FOV and same resolution Δw . **1.6b** keeping Δk the same and decreasing k_{max} by half, produces an image of the same FOV and lower resolution Δw

which makes the spins far from the center precess at higher frequencies compared to than the center ones, producing a signal low in amplitude.

The simplest way of filling the K-space is to define a constant Δk per dimension. This makes the image reconstruction a simple step of just performing an Inverse Fast Fourier Transform. Different trajectories that exploit the characteristics of the K-space more efficiently have been proposed. Nevertheless, these type of trajectories, do not have an equal spacing Δk per dimension, for this reason, the image cannot be reconstructed with a simple FFT algorithm. Two of the most common non-Cartesian trajectories are spiral and radial. A diagram can be found in figure 1.7.

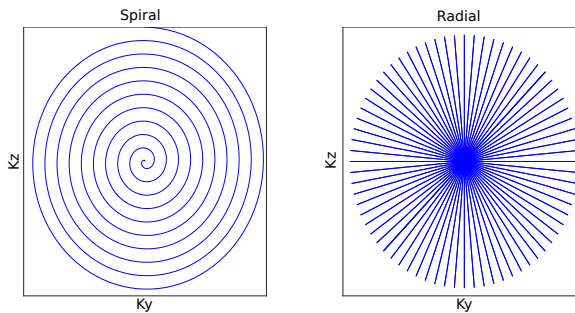


Figure 1.7: Non-Cartesian K-space trajectories: Spiral and radial trajectories

1.1.4. IMAGE RECONSTRUCTION

As mentioned in the previous section, the signal acquisition can be performed either in a Cartesian or non-Cartesian matter. For the Cartesian one, the image can be obtained using a simple Inverse Fast Fourier Transform algorithm. On the other hand, a

more complex algorithm is needed to reconstruct non-Cartesian acquisitions. One approach is to use a Non-Uniform Fast Fourier Transform algorithm [8], which uses interpolation techniques to convert the non-uniform K-space data into an equally spaced points and then apply an FFT algorithm to the interpolated data. When using Parallel Imaging techniques and non-Cartesian K-space trajectories, image reconstruction can also be performed iteratively, solving an optimization problem.

1.1.5. PARALLEL IMAGING

As previously mentioned, MRI is considered a slow medical imaging technique. Compared to others like CT or Ultrasound, the time needed to acquire signals and generate an image is significantly longer. Several methods have been proposed to accelerate the acquisition time in MRI. As equation 1.17 suggests, one way to reduce the imaging time is by reducing the number of phase encoding steps, this implies that the distance Δk , equation 1.19, between sampling points in the K-space is increased, skipping K-space lines is also called under-sampling. In the image domain, this results in a reduction of the FOV, generating aliasing in the image as explained in subsection 1.1.3. The amount of data reduction (phase encoding steps reduction) is called the acceleration factor $R = R_y \times R_z$ and is defined as the ratio between the number of K-space points in the fully-sampled data and the under-sampled one, R_y and R_z are the under-sampling factors in the phase and slice encoding respectively. Parallel Imaging or PI is a technique that allows the reconstruction of an almost artifact-free image from under-sampling the K-space [9].

PI requires specialized receive coil arrays, which are composed of several independent receiver channels, one for each coil, an example of this coils can be found in figure 1.8b. Since each of these coils are in a different position, they have different sensitivity to the area being imaged compared with the others as in can be see in figure 1.8a. This different sensitivity can be used as extra spatial information in the reconstruction problem since each of the coils will receive the same signal with different intensities. This way, a full image can be reconstructed even if the number of phase encoding steps is reduced.

Different methods can be used to retrieve the underlying magnetization from the under-sampled data and the coil sensitivity profiles. Sensitivity Encoding SENSE [10] and GenerAlized Autocalibrting Partial Parallel Acquisition GRAPPA [11] are two of the most commonly used. The first one separates the aliased pixels in the image domain, whereas the latter reconstructs the missing K-space lines. Both methods need to solve a set of equations. This work uses SENSE to reconstruct the under-sampled images.

The basic idea of SENSE reconstruction is that an image can be reconstructed without significantly affecting its quality, even if the K-space is under-sampled. As shown in figure 1.6a, under-sampling the K-space produces a reduced FOV image with aliased pixels. SENSE uses the different coil sensitivities of each receiver channel as extra spatial information, each coil will generate an incomplete image that can further be combined in a process called unfolding, to arrive to the full FOV image, a visual representation can be found in figure 1.8b. The key for signal separation is that each of the single-coil image signal super-positions happens with different weights according to the local coil sensitivities. The signal separation is achieved by solving:

$$v = Ua \tag{1.22}$$

Where \mathbf{v} is the resulting vector listing the separated pixel values from the original superimposed ones, \mathbf{a} is a vector containing the image values of the intermediate images (reduced FOV), U is the unfolding matrix used to perform signal separation and is given by:

$$U = (S^H \Psi^{-1} S)^{-1} S^H \Psi^{-1} \quad (1.23)$$

Where the sensitivity matrix S contains the complex coil sensitivity maps as found in figure 1.8b, and Ψ is the noise receiver matrix that describes the levels and correlation of noise in the receiver channels.

An essential concept in Parallel Imaging is the so-called geometry factor or ***g-factor***, which is a measure of noise amplification. This noise amplification occurs when the coil sensitivities from different channels have similar values in the same location, making the unfolding matrix inversion problem ill-conditioned. To solve the system of equations, the matrix has to be inverted, one of the characteristics of this inversion is that when the equations composing the matrix are similar, it will produce solutions extremely sensitive to small variations in the data, in this case this variation is the random noise in the acquired K-space data. Thus, this noise is amplified in the reconstructed image when the sensitivities from different channels have similar values in the same location. The g -factor values are always ≥ 1 , depending on the distribution of the g -factor and the application, acceptable values are below 1.2 [12].

Both the design of the receive coils and the K-space trajectory can be used to reduce the g -factor penalty. For uniformly under-sampled Cartesian trajectories, the noise after reconstruction will be distributed consistently in the image domain. In contrast, for non-Cartesian acquisitions, a non-uniform distribution of noise will be present in the K-space data, and a different noise distribution in the image domain appears. For this reason, non-Cartesian acquisitions are best suited for PI techniques. The general form to calculate the g -factor is:

$$g_\rho = \sqrt{[(S^H \Psi^{-1} S)^{-1}]_{\rho, \rho} (S^H \Psi^{-1} S)_{\rho, \rho}} \geq 1 \quad (1.24)$$

Where S is the sensitivity matrix, Ψ represents the noise correlation matrix, and the subscript ρ represents the two dimensional position vector $\rho = (x, y)$ in the image.

Furthermore, as is often said, there is "no free lunch" in MRI, in this case the speed up in acquisition time reduces the overall Signal to Noise Ratio in the image, equation 1.18 is modified and yields the expression for the SNR in accelerated Parallel Imaging:

$$SNR_{accelerated(x,y)} = \frac{SNR_{full}(x,y)}{g(x,y)\sqrt{R}} \quad (1.25)$$

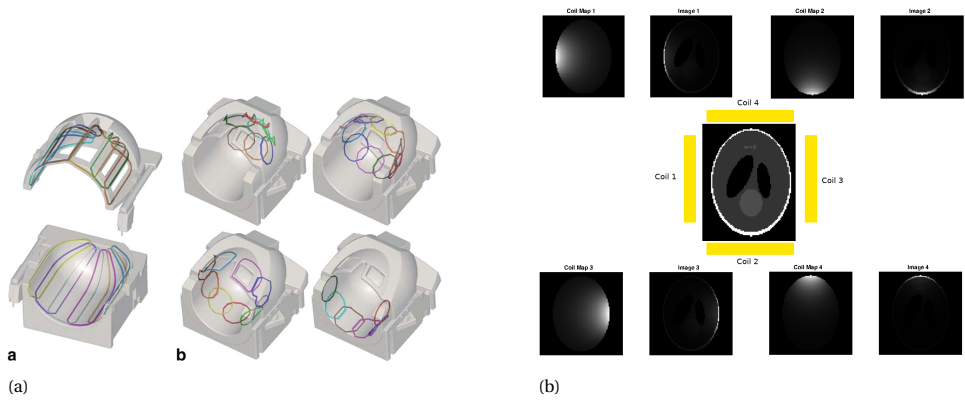


Figure 1.8: Parallel Imaging, 1.8a example of receiver coil arrays used for PI, reprinted from [13] and 1.8b simplified graphical representation of SENSE, each coil generates a partial image which together can be combined into a full image

2

HEAD INSERT GRADIENT COIL

As described in chapter 1, the gradient coil system is used to spatially encode the acquired signal. The slice selection, frequency encoding and phase encoding steps have to be repeated several times in order to acquire all the signals required to reconstruct the image. It is for this reason, that a gradient coil that can be switched on and off faster will decrease the total imaging time.

The gradient field is produced by passing an electrical current through coil arrangements. An efficient gradient coil system generates a gradient field with minimum stored magnetic energy, which will allow it to be switched rapidly. The way to achieve this is by designing a coil that has low inductance and small resistance [14]. In general for MRI, the higher the achievable gradient magnetic field strength, the better. The magnetic field strength is given by:

$$G = \eta I \quad (2.1)$$

Where I is the applied current and η is the efficiency of the coil that its mainly influenced by the geometry of the coil. In general, the smaller the coil radius, the more efficient it is. An important characteristic of this type of coils is the rise time, the time a gradient coil takes to achieve its peak gradient strength, the shorter this time, the faster the coil can be switched, rise time is defined by:

$$\tau = \frac{LI}{V - RI} \quad (2.2)$$

Where L is the inductance, R resistance of the coil, I and V the maximum current and voltage supplied by the gradient amplifier. A common way to evaluate the performance of a gradient coil is by means of its **Slew Rate**, which is the ratio between the maximum gradient strength and the rise time:

$$SR = \frac{G_{max}}{\tau} = \frac{\eta(V - RI)}{L} \quad (2.3)$$

To address the gradient coil design parameters explained above a high efficiency insert coil that outperforms conventional gradient systems was developed [4]. A comparison of the main characteristics of this coil versus a conventional one can be found in table 2.1. It can be seen that the maximum gradient amplitude and Slew Rate of the insert gradient coil is significantly higher than conventional gradient systems, this allows the coil to be switched in higher rates and thus allow shorter TR and acquisition times. An image of the coil developed at the University Medical Center Utrecht can be found in figure 2.1.

	Slew Rate (T/m/s)	Max G (mT/m)
Insert coil normal frequencies	1,300	200
Conventional gradient	150-200	20-45

Table 2.1: Comparison of gradient coil specifications



Figure 2.1: Head insert gradient coil developed at the UMC Utrecht

3

WAVE-CAIPI

Wave-CAIPI [3] is a 3D parallel imaging method that allows higher under-sampling factor R and lower g -factor penalty compared with other Parallel Imaging techniques, and it can be applied to any scan protocol. This method combines 2D CAIPIRINHA [15] and Bunched Phased Encoding [16] strategies. It consists of playing sinusoidal gradients on the phase encoding directions during readout and generating inter-slice shifts. The effect of playing this sinusoidal can be interpreted as an extra phase deposited in each readout line; this translates into a corkscrew trajectory in the K -space. When acquiring the Wave-CAIPI under-sampled data, it can be seen that the effect of the sinusoidal gradients in the image is spreading the voxels in all three dimensions; this way, the 3D sensitivity of the receiver coil is used, and the quality of the reconstructed image improves. Reconstructing the underlying image from the under-sampled data can be seen as solving the system of equations in a SENSE model as in section 1.1.5 and is performed iteratively using as an input, the coil sensitivities, point spread functions, and the acquired wave images. This section presents a brief introduction to 2D CAIPI and BPE, followed by the mathematical formulation of the WAVE-CAIPI method.

3.1. 2D CAIPIRINHA AND BUNCHED PHASED ENCODING

The Controlled Aliasing in Parallel Imaging Results in Higher Acceleration or 2D CAIPIRINHA method modifies the trajectory in the under-sampled K -space. This way, the aliased pixels are shifted in a controlled manner. This effect is achieved by changing the phase encoding gradients in every readout line to be able to shift the collapsed pixels. Figure 3.1 shows the pulse sequence diagram, K -space trajectory, and how the collapsed pixels can be shifted in the spatial domain image.

The method of Bunched Phased Encoding or BPE, uses a zigzag sampling trajectory, and an increased number of readout samples are acquired, allowing to reduce scan time. The zigzag trajectory is achieved using an oscillating phase encoding gradient during readout. This method shows that the phase Encoding step size can be set higher than the conventional used $1/FOV$, equation 1.19, the effect of the trajectory along with the

increased sampling rate is similar to acquiring multiple Phase Encoding lines in a single readout. Figure 3.2 shows an example of the sequence diagram, K-space trajectory, and under-sampled time-domain image.

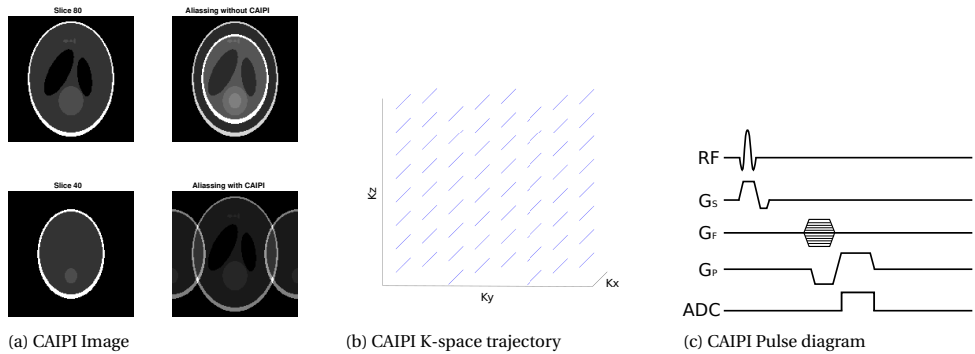


Figure 3.1: 2D CAIPI strategy, 3.1a CAIPI vs non-CAIPI aliasing, 3.1b K-space trajectory and 3.1c pulse sequence diagram

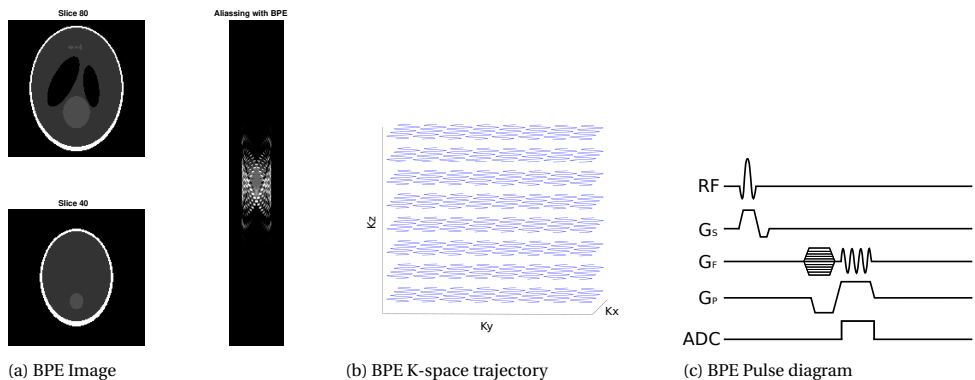


Figure 3.2: Bunched Phased Encoding strategy, 3.2a BPE aliasing, 3.2b K-space trajectory and 3.2c pulse sequence diagram

3.2. WAVE-CAIPI

Wave-CAIPI uses the principles of 2D-CAIPIRHHHA and BPE to take full advantage of the receiver coils 3D sensitivities. In 3D acquisitions, the encoding strategy is modified in a 2D-CAIPI matter, so the aliasing is reduced, and the spatial sensitivity is better exploited. Additionally, sinusoidal gradients with a $\pi/2$ phase shift are applied in the phase encoding directions during readout. The combined effect results in a corkscrew trajectory in the K-space, which generates a reduced FOV image where the pixels are spread out in all three dimensions. A SENSE reconstruction scheme is used to obtain the underlying image.

The signal equation when playing additional sinusoidal wave gradients in the phase encoding y and partition encoding z directions is given by:

$$s(t) = \int_{x,y,z} m(x, y, z) e^{-i2\pi(k_x(t)x + k_y y + k_z z)} \exp\left(-i\gamma \int_0^t (g_y(\tau)y + g_z(\tau)z) d\tau\right) dx dy dz \quad (3.1)$$

Where m is the magnetization, k_x , k_y and k_z are the values in the K-space, x , y and z are the coordinates in the image domain, g_y and g_z are the phase encoding gradient waveform applied and γ is the gyromagnetic ratio. Equation 3.1 can be discretized as:

$$\text{wave}[x,y,z] = \sum_k e^{i2\pi kx/N} \left(e^{-2\pi(P_y[k]y + P_z[k]z)} \sum_x m[x,y,z] e^{-i2\pi kx/N} \right) \quad (3.2)$$

The effect of the wave gradients can be interpreted as a convolution of each readout line with a Point Spread Function (PSF), which describes how the pixels are spread out, this can be seen in figure 3.4. Using this representation, the forward model for Wave-CAIPI is a multiplication in K-space or a convolution in image space, so equation 3.2 can be written as:

$$\text{wave}[x,y,z] = \mathbf{F}_x^{-1} \text{Psf}[x,y,z] (\mathbf{F}_x m[x,y,z]) \quad (3.3)$$

Where the PSF is given by:

$$\text{Psf}[x,y,z] = e^{-i2\pi(P_y[k]y + P_z[k]z)} \quad (3.4)$$

$$P_y(t) = \frac{\gamma}{2\pi} \int_0^t g_y(\tau) d\tau \quad (3.5)$$

$$P_z(t) = \frac{\gamma}{2\pi} \int_0^t g_z(\tau) d\tau \quad (3.6)$$

$g_y(\tau)$ and $g_z(\tau)$ are the applied time-varying gradients, for Wave-CAIPI this sinusoidal gradients with a $\pi/2$ phase difference. Figure 3.3 shows an example of the sequence diagram, K-space trajectory and under-sampled time domain image.

There are five acquisition parameters that influence how the pixels of the Wave-CAIPI image are spread out, in this work we call them Wave-CAIPI parameters, this parameters can be found in the following table:

Name	Unit	Description
Gy	mT/m	Max amplitude of sine gradient in phase encoding direction (y)
Gz	mT/m	Max amplitude of cosine gradient in slice direction (z)
Sinsy	cycles	Number of cycles in phase encoding direction (y)
Sinsz	cycles	Number of cycles in slice direction (z)
p_{bw}	Hz	Pixel bandwidth

Table 3.1: Wave-CAIPI parameters

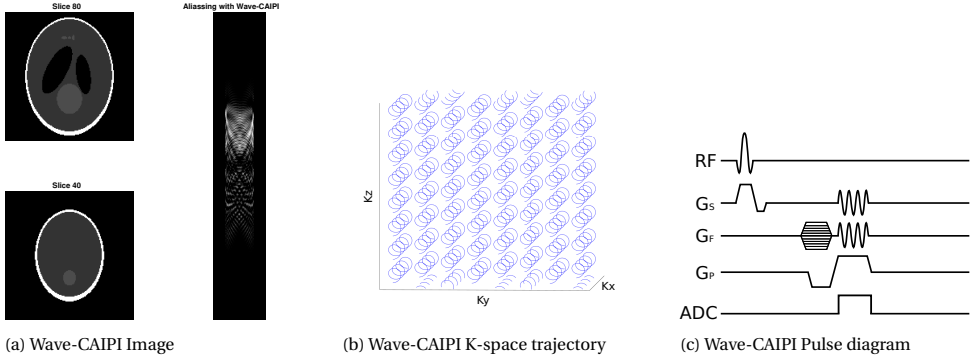


Figure 3.3: Wave-CAIPI strategy, 3.3a Wave-CAIPI aliasing, 3.3b K-space trajectory and 3.3c pulse sequence diagram

3.3. IMAGE RECONSTRUCTION

As explained in the parallel imaging section 1.1.5, when an R acceleration factor in the phase and partition encoding is used, columns of pixels will collapse on top of each other and can be unfolded using the Coil Sensitivity map that describes the field of view of each of the receiver coils in the multi-channel receiver coil array. Starting from equation 3.2 and incorporating the Coil Sensitivities, the following system of equations represent the collapsed columns and the under-laying magnetization:

$$\begin{bmatrix} F^{-1}Psf[y_1]FC_1[y_1] & \dots & F^{-1}Psf[y_p]FC_1[y_p] \\ \vdots & \ddots & \vdots \\ F^{-1}Psf[y_1]FC_n[y_1] & \dots & F^{-1}Psf[y_p]FC_n[y_p] \end{bmatrix} \begin{bmatrix} m[y_1] \\ \vdots \\ m[y_p] \end{bmatrix} = \begin{bmatrix} wave_1 \\ \vdots \\ wave_n \end{bmatrix} \quad (3.7)$$

Where F denotes a 1D Fourier transform, Psf , C and m represent the Point Spread function, Coil Sensitivity and underlying magnetization respectively, the indices $[y]$ the collapsed columns, $wave$ represents the acquired Wave-CAIPI image and the sub-index n counts the number of coils in the receiver array. The system of equations in 3.7 can be seen as a direct SENSE model, where the acquired non-Cartesian data is related to the underlying image:

$$Ei = k \quad (3.8)$$

E is the encoding matrix constructed from Point Spread Function and the Coil Sensitivities, i is the underlying image, and k is the acquired K-space data. Equation 3.8 can be solved in an iterative matter, solving the following optimization problem:

$$\min \|k - Ei\|_2 \quad (3.9)$$

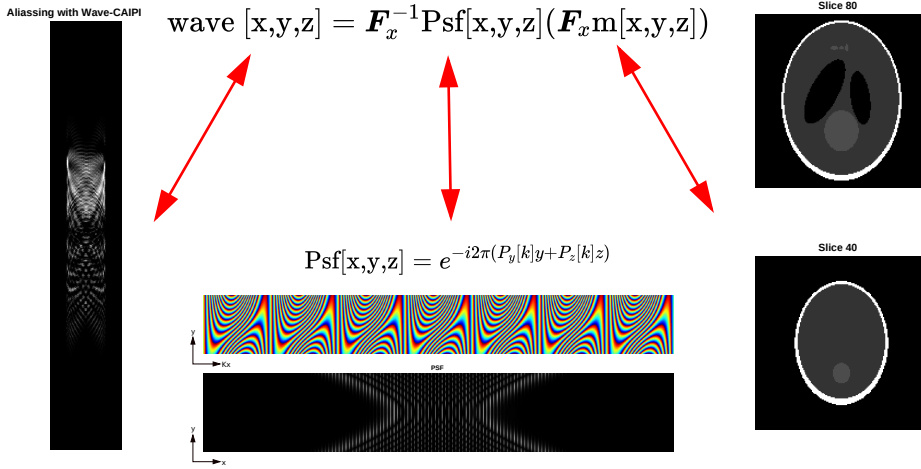


Figure 3.4: Wave-CAIPI equation and visual representation of each component of it.

The effect of multiplying the the magnetization m with the PSF is a spreading of each pixel in the readout direction, following the shape of the PSF in the image domain (center down picture). Left: Wave-CAIPI image; center up: Point Spread Function in the hybrid K-space (K_x, y); center down: PSF in the image domain (x, y), it describes the spreading effect in the readout direction (x); right: two different slices of the Shepp-Logan phantom.

3.4. QUALITY ASSESSMENT

Three different measurements of the quality of the reconstructed image are typically used to assess the performance of Wave-CAIPI, **average g-factor**, **max g-factor** and **Normalized Root Mean Squared Error**. In order to calculate the g-factor, equation 1.24 is modified to incorporate the PSF information, arriving to equation 3.10 from where the average G-factor 3.10 and maximum G-factor 3.11 can be calculated. The Normalized Root Mean Squared Error NRMSE, equation 3.12 is a measure of the quality of the reconstruction and is useful to quantify the artifacts and noise in the final image.

$$g_{\text{av}} = \frac{1}{N} \sum_{\rho=1}^N g_{\rho} \quad \text{where} \quad g_{\rho} = \sqrt{(E^H E)_{\rho, \rho}^{-1} (E^H E)_{\rho, \rho}} \quad (3.10)$$

$$g_{\text{max}} = \max(g_{\rho}) \quad (3.11)$$

$$\text{NRMSE} = \frac{\text{MSE}}{\text{median}(\hat{M}_{\rho})} \quad \text{where} \quad \text{MSE} = \frac{1}{N} \sum_{\rho=1}^N (M_{\rho} - \hat{M}_{\rho})^2 \quad (3.12)$$

Where ρ represents the index of the g factor values in the Region of Interest, N is the total number of ρ , and \hat{M} is the reconstructed image. The g-factor is usually presented in the so-called g-factor map, which allows to identify the sections where the noise might be amplified, such as the one in figure 3.5.

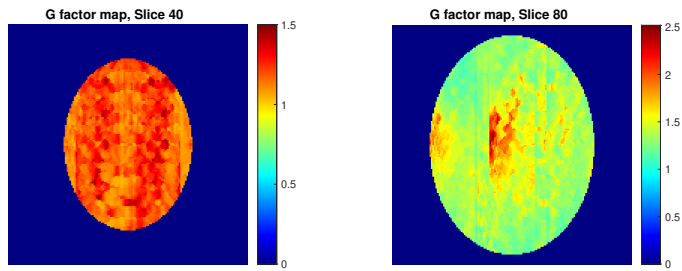


Figure 3.5: Example of G-factor map of a 160x160x160 phantom with R=4x4 under-sampling factor

4

METHODS

The feasibility of using a Wave-CAIPI strategy with the described high-performance gradient insert coil was investigated with several simulations, the steps used to simulate this process are presented in section 4.1. In addition, the Wave-CAIPI sequence was implemented on a 7T scanner, which allowed to validate the simulations with real-life data. This process is described in section 4.3.

4.1. SIMULATIONS

The first part of this project included several simulations. To begin with, the Wave-CAIPI method was implemented in MATLAB R2019b; the steps followed for these simulations are explained in subsection 4.1.1. To investigate how the different Wave-CAIPI parameters 3.1 affect the reconstruction, three different tests were performed. Firstly, we looked for a relation between the Range of Spread, equation 4.8, and G-average, G-max and RMSE. Secondly, the effect that the number of sine cycles has in the construction was investigated. Thirdly, the effect of the pixel bandwidth was explored. The possible time gain when using the insert gradient coil compared with conventional gradient systems was also evaluated, the processes followed is further developed in subsection 4.2.4.

4.1.1. WAVE-CAIPI METHOD SIMULATION

As it can be seen from equation 3.7, three components are needed to reconstruct the image, the Coil Sensitivity, the Point Spread Function and the under-sampled Wave-CAIPI image. Adapting the original proposed reconstruction algorithm available online [3] to reconstruct different under-sampling factors and image sizes, a reconstruction algorithm that takes as an input the Point Spread Function, Coil Sensitivity Map and Wave-CAIPI image to find the original image was developed. The steps followed to simulate the image and reconstruction can be found in table 4.1

1. Several parameters which define the characteristics of the simulated data are selected. These parameters describe important aspects of the scan session such as image Field of View, pixel bandwidth, matrix size, read-out time, total scan time,

Step	Description
1.	Select parameters
2.	Calculate oversampling factor
3.	Generate 3D phantom
4.	Coil sensitivity
	a. Using Biot-Savart law
	b. Using data from scanner and BART toolbox
5.	Generate image per receiver channel
6.	Simulate Point Spread Function
7.	Simulate Wave-CAIPI image
	a. Using NUFFT and corkscrew trajectory
	b. Using PSF and phantom

Table 4.1: Methods steps, simulation of Wave-CAIPI methodology

Name	Unit	Description
N_x		Number of pixels in readout (x)
N_y		Number of pixels in the phase encoding direction (y)
Sl		Number of pixels in slice direction (z)
G_y	mT/m	Max amplitude of sine gradient in phase encoding direction (y)
G_z	mT/m	Max amplitude of cosine gradient in slice direction (z)
$Sins_y$	cycles	Number of cycles in phase encoding direction (y)
$Sins_z$	cycles	Number of cycles in slice direction (z)
p_{bw}	Hz	Pixel bandwidth
R_y		Under-sampling factor in phase encoding direction (y)
R_z		Under-sampling factor in slice direction (z)
p_s	mm	Vector with pixel size [x,y,z]

Table 4.2: Initial parameters for Wave-CAIPI simulations

the under-sampling factor and Wave-CAIPI parameters. A summary can be found in table 4.2

2. The oversampling factor defines the number of samples needed to make sure no information is lost due to the spreading effect of the wave gradients.
3. A Shepp-Logan phantom and an image of a brain scan were used in the simulations. The phantom was used to mimic a real-life brain, some slices of the fully sampled brain and phantom are presented in figure 4.1. This phantom consists of various ellipsoids with different intensities which is analogous to the structure of a brain. The size of this phantom is defines by the Field of View given by $N_x \times N_y \times Sl$.
4. As explained in chapter 3, the coil sensitivity is a matrix of weights that describes the sensitivity of each coil in an array and gives extra spatial information that is used to reconstruct the image with under-sampled data. Two different approaches were used to simulate the coil sensitivities:
 - (a) Coil sensitivity maps were simulated, using the Biot-Savart law and parameters to specify the physical dimensions of the receiver coil, figure 4.3a
 - (b) Coil sensitivity maps were obtained using the BART toolbox [17] and sensitivities from other phantom acquisition in the scanner, figure 4.2b

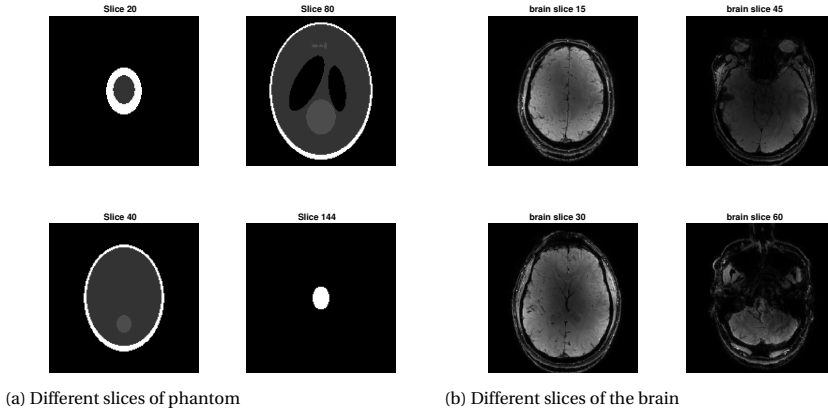


Figure 4.1: Volumes used to test reconstruction, [4.1a](#) Shepp-Logan phantom, [4.1b](#) volunteer's brain

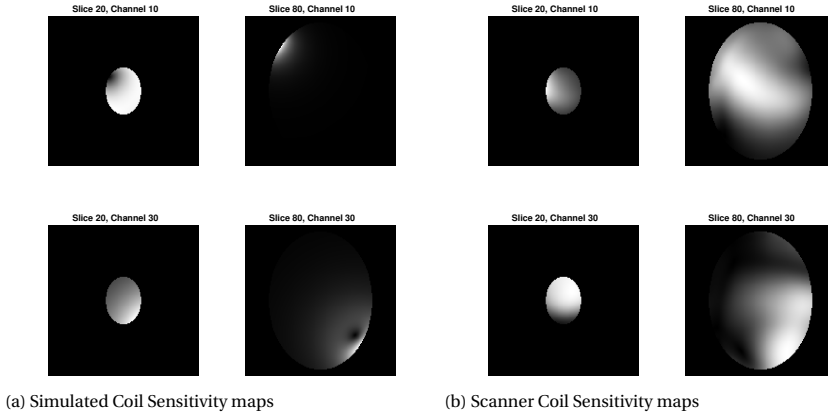


Figure 4.2: Coil Sensitivity maps, [4.3a](#) simulated and [4.2b](#) calculated from scanner using BART toolbox [17]

5. To simulate an image per each channel of the receiver coil, the phantom from 3 was multiplied with the coil sensitivity map from 4. Some slices and channels can be found in figure [4.3](#).
6. The Point Spread function defines the effect of the sinusoidal gradients played during readout and it is defined by equation [3.4](#). It is simulated with the following steps:
 - (a) A Cartesian grid of points for the y and z grid in image domain is created
 - (b) PSF of Y and Z gradients are calculated with equations [3.5](#) and [3.6](#)
 - (c) PSF of Y and Z gradients are combined to arrive to PSF YZ that represents the effect of both phase and slice gradients applied during readout, equation [3.4](#)

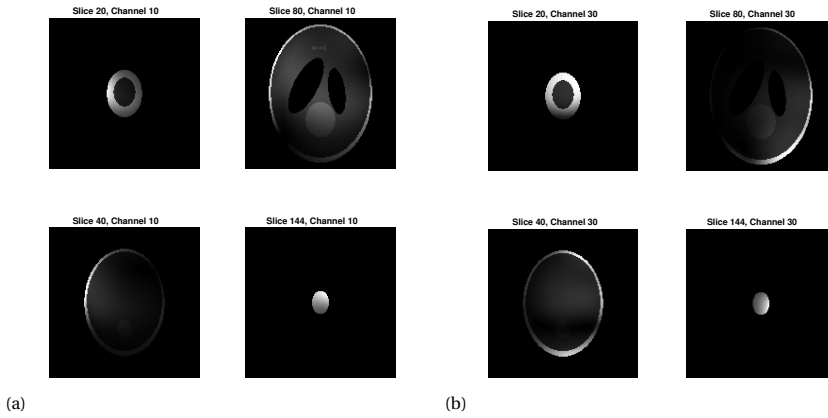


Figure 4.3: Reconstructed image, slices 20 and 80, channels 10 and 30 of scanner coil sensitivity

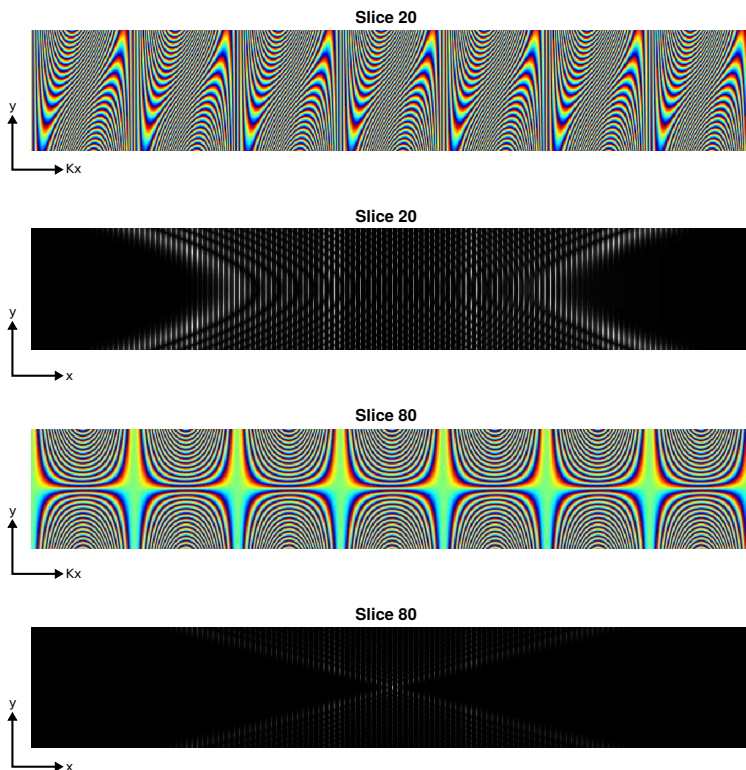


Figure 4.4: Point Spread Function, slices 20 and 80, hybrid K-space (K_x, y) and image domain (x, y) representations

7. Two different approaches were used to simulate the Wave-CAIPI image. The first one uses a Non-Uniform FFT algorithm [18] to calculate the values of the K-space data in the simulated trajectory:

(a) The corkscrew like K-space trajectory is simulated, using the parameters from point 1.

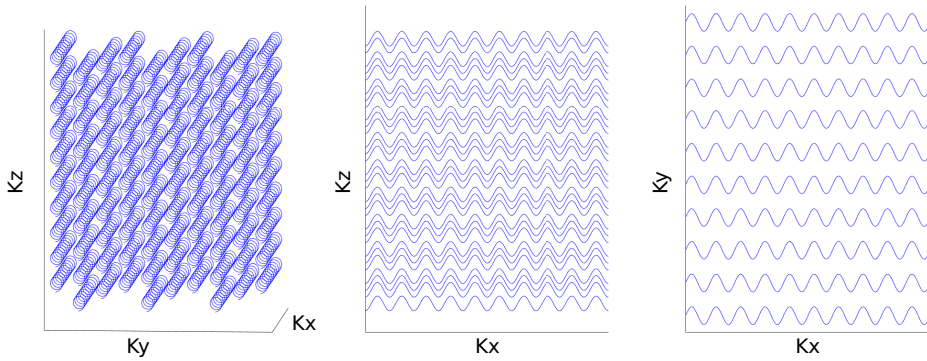


Figure 4.5: Simulated under-sampled Wave-CAIPI trajectory in K-space

(b) The values of the simulated K-space points are calculated using a Non-Uniform FFT algorithm. It takes as an input the phantom values obtained from 5 and the coordinates of the simulated K-space trajectory from point 6. To speed up this calculation a gpuNUFFT function [18] was used.

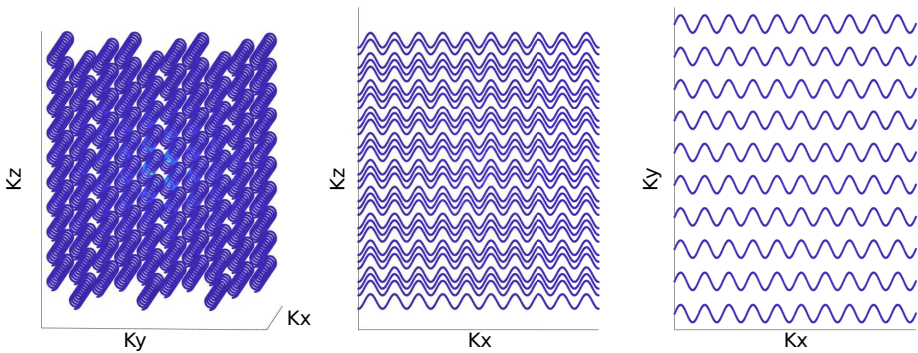


Figure 4.6: Under-sampled K-space values of trajectory obtained from the NUFFT

(c) Zeros are added to the data matrix obtained from 7 in a CAIPI like pattern [15] and making sure the desired FOV is obtained, an example can be seen in figure 4.7.

- (d) To better simulate the K-space data, noise is with an SNR of 20 dB is added to the data.

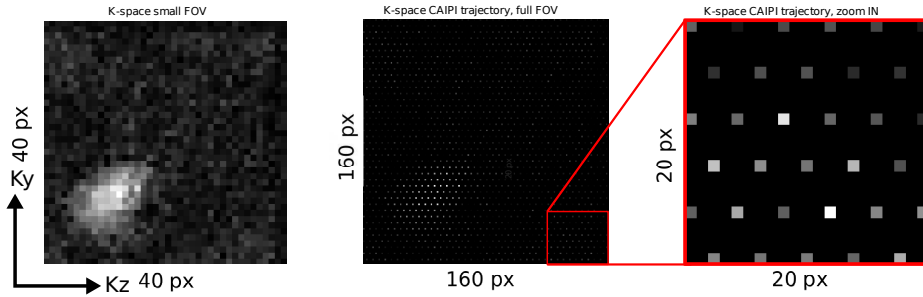


Figure 4.7: K-space NUFFT, zeros are added to the reduced FOV data in a 2D CAIPI fashion. Left: matrix of the reduced FOV K-space 40x40 px; center: matrix of the full FOV (zeros added in a CAIPI way) 160x160 px; right: zoom in to matrix, CAIPI strategy is visible

- (e) An 3D Inverse Fourier Transform is applied to the data matrix.
 (f) The simulated Wave-CAIPI image is obtained.

The second approach uses the simulated PSF and the definition of Wave-CAIPI image that states that the image is a multiplication of the image with the PSF, the following steps were followed to obtain the image using this definition, figures 4.8 and 4.9 show this process:

- (a) Zeros are padded in the readout direction (x) to the phantom image, to match the length of the psf with the oversampling factor.
- (b) A 1D FFT in the readout direction (x) is taken to the image obtained in 6, this brings it to the hybrid K-space.
- (c) The PSF is multiplied with the image obtained from (b)
- (d) To better simulate the K-space data, noise with an SNR of 20dB is added to the data.
- (e) A 1D inverse FFT in the readout direction is taken to the image from (d).
- (f) To arrive at the desired FOV, with under-sampling, the image from (e) is cropped.
- (g) The simulated Wave-CAIPI image is obtained.

After the Coil Sensitivity map (4), Point Spread Function (6), and Wave-CAIPI image (7) have been simulated, the reconstruction can be performed. The reconstruction consists of solving the linear system of equations in equation 3.7 and is done iteratively solving the optimization problem in equation 3.9.

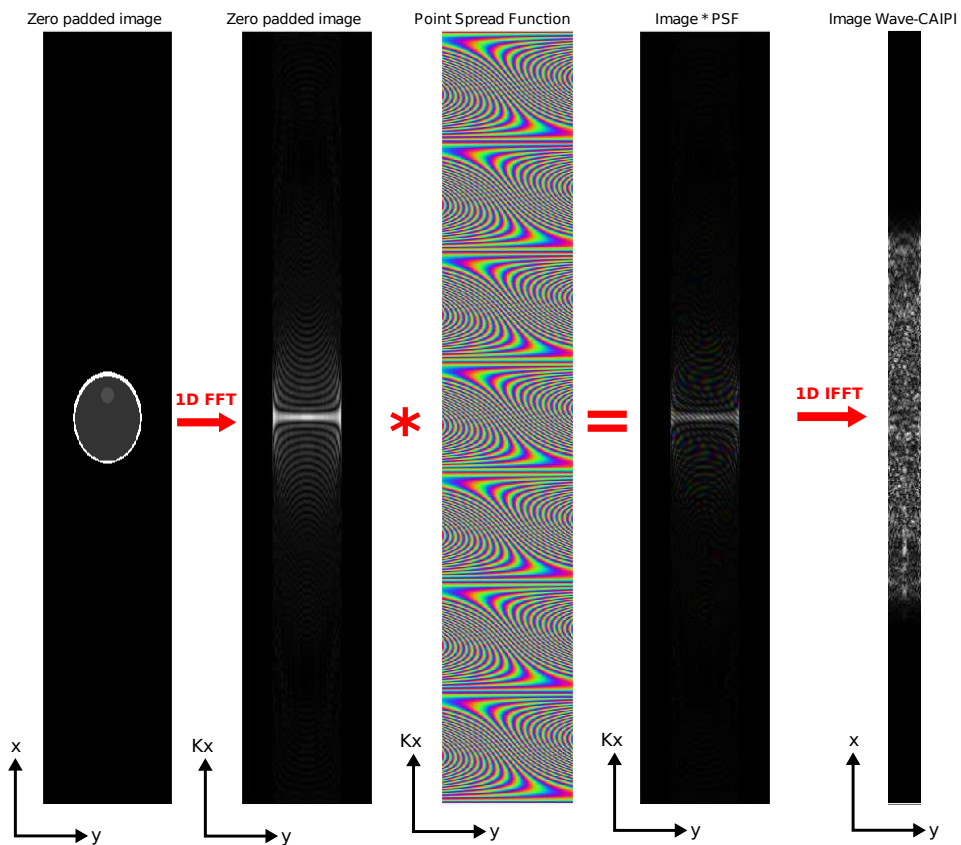


Figure 4.8: Phantom Wave-CAIPI image formation, the zero padded image is multiplied by the PSF in the hybrid K-space (Kx, y), after applying an IFFT and crop the image to the under-sampled size, we arrive at Wave-CAIPI image

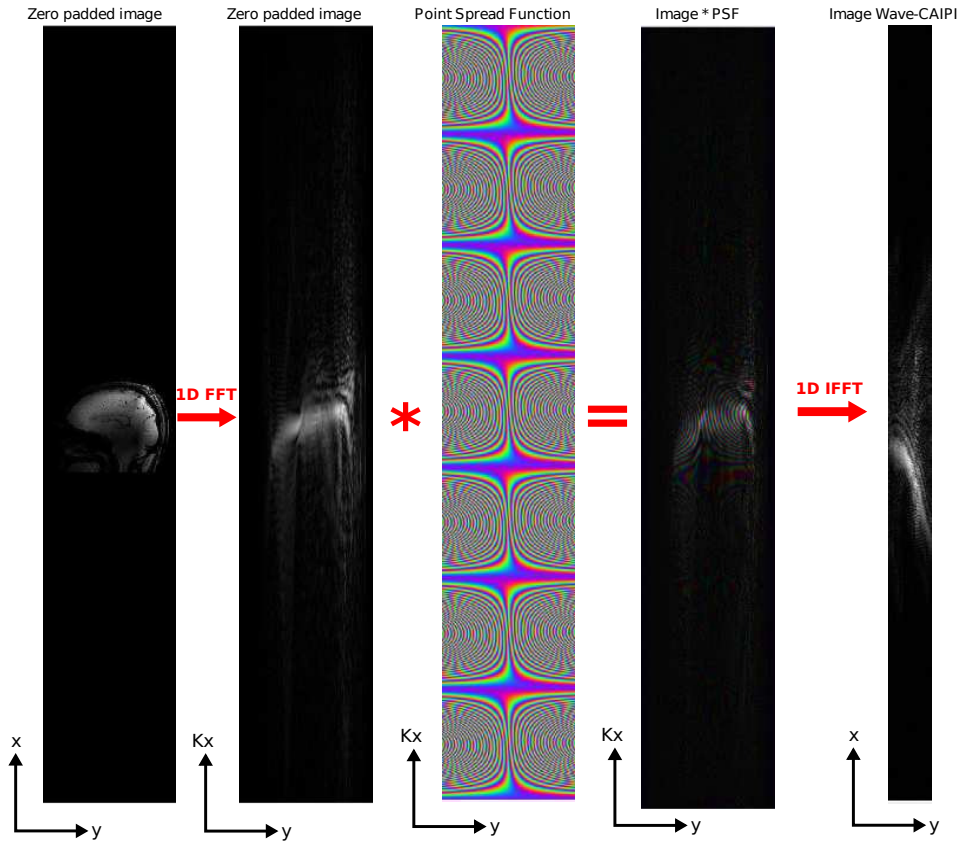


Figure 4.9: Brain Wave-CAIPI image formation, the zero padded image is multiplied by the PSF in the hybrid K-space (Kx, y), after applying IFFT and crop the image to the under-sampled size, we arrive at Wave-CAIPI image

4.1.2. QUALITY ASSESSMENT

As stated in section 3.4, to assess the quality of the reconstructed image, three metrics were used: average G-factor, max G-factor, and NRMSE. The three metrics are calculated as follow:

$$g_{\text{av}} = \frac{1}{M} \sum_{\rho=1}^M g_{\rho} \quad \text{where} \quad g_{\rho} = \sqrt{(E^H E)_{\rho,\rho}^{-1} (E^H E)_{\rho,\rho}} \quad (4.1)$$

$$g_{\text{max}} = \max(g_{\rho}) \quad (4.2)$$

Where ρ represents the position in the image of each g-factor values of the ROI, M counts the total number of ρ positions, and \hat{M} is the reconstructed image. E is the $n_c n_k \times N^2$ Encoding matrix, n_c is the number of channels, n_k sampling points and is given by:

$$E = \begin{bmatrix} F^{-1} P s f [y_1] F C_1 [y_1] & \dots & F^{-1} P s f [y_p] F C_1 [y_p] \\ \vdots & \ddots & \vdots \\ F^{-1} P s f [y_1] F C_n [y_1] & \dots & F^{-1} P s f [y_p] F C_n [y_p] \end{bmatrix} \quad (4.3)$$

The columns of this matrix represent the collapsed columns due to under-sampling and 2D CAIPI pattern. To obtain the Encoding matrix, first, the full Encoding matrix is calculated (all pixels in the image). This full matrix is further subset with the collapsed columns due to under-sampling and 2D CAIPI pattern (collapsed pixels). Acceptable values for average g-factor are in the range of 1-1.2 [19].

The Normalized Mean Squared Error, measures the difference between the simulated phantom and the Wave-CAIPI reconstruction, it is calculated as follows:

$$\text{NMSE} = \frac{\text{MSE}}{\text{median}(\hat{M}_{\rho})} \quad \text{where} \quad \text{MSE} = \frac{1}{N} \sum_{\rho=1}^N (M_{\rho} - \hat{M}_{\rho})^2 \quad (4.4)$$

Where ρ is the index of the non-zero pixels in the images, N counts the number ρ pixels, M is the simulated image of the phantom and \hat{M} is the reconstructed image.

4.2. PARAMETERS OPTIMIZATION

As mentioned in section 3.2, five different Wave-CAIPI parameters affect the quality of the reconstruction. Previously Polak [20] empirically found that the amplitude of the gradients and pixel bandwidth defines the amount of spreading in the image. In general, higher gradient amplitudes and smaller the pixel bandwidth generate more spreading. This is translated into a lower g-factor penalty (noise amplification), allowing a better reconstruction. Polak also found that increasing the number of sine cycles does not significantly increase the spreading, but reduces the artifacts present in the reconstructed image. These findings were confirmed and mathematically described in [21], where it is concluded that not necessarily the higher amplitude and higher number of sine cycles would produce the best reconstruction. A fast g-factor calculation method was also presented in the same work, equation 4.5, which partially holds when the g-factor is close to unity, such as in the case of R=3x3 under-sampling.

$$g_{mean} \approx 1 + \eta(g_c - 1) \quad (4.5)$$

Where η is a coefficient depending on settings of the acquisition, it was empirically found that 0.37 creates good approximations and g_c is the g factor value on the central position, which can be calculated by:

$$g_c = \sqrt{(e_c^H d)(S^H S)_{c,c}} \quad (4.6)$$

$$(E^H E)d = e_c \quad (4.7)$$

Where e_c is a vector of all zeros with one in the central position, E is the encoding matrix and d is calculated solving iteratively the system of equations 4.7.

This work does not use this optimization approach for two reasons. Firstly, we allow more degrees of freedom in choosing the Wave-CAIPI parameters and secondly, we investigate the quality of the reconstruction for a under-sampling factor of R=4x4, which has not been proved to be close to unity, so the fast calculation method cannot be directly applied to the framework presented in this thesis. To find out how the Wave-CAIPI parameters affect the reconstruction, the effect of the range of spread, number of cycles and pixel bandwidth was investigated separately.

4.2.1. RANGE OF SPREAD EFFECT

A parameter optimization problem was formulated in [21], which attempts to find the optimal gradient amplitude to have a proper image reconstruction. This optimization problem assumes that the same gradient amplitude and sine cycles are applied in Y and Z direction. In this work, more degrees of freedom are allowed, so G_y and G_z as well as $Sinsy$ and $Sinsz$ do not necessarily need to be equal. The additional degrees of freedom make the optimization problem more complex. For this reason, it was decided to optimize the parameters performing simulations.

A concept introduced in [21], the range of spread, was used since it incorporates all the different Wave-CAIPI parameters that affect the reconstruction. It is calculated as:

$$R_g = \frac{2 \cdot \max(F_{inst})}{p_{bw}} + Nx \quad (4.8)$$

Where p_{bw} is the pixel bandwidth, Nx is the number of pixels in the readout direction (x) the instantaneous frequency F_{inst} is given by:

$$F_{inst} = -\gamma(G_y \cos(\omega_y t) y + G_z \sin(\omega_z t) z) \quad (4.9)$$

$$\omega_y = 2\pi(Sinsy)(p_{bw}) \quad \text{and} \quad \omega_z = 2\pi(Sinsz)(p_{bw}) \quad (4.10)$$

As it can be seen in figure 4.10 the maximum instantaneous frequency is a good approximation of the spread out in the readout direction.

Extensive simulations were performed to find the Wave-CAIPI parameters that minimize the g-factor and NRMSE. The range of spread, equation 4.8 was calculated for different combinations of parameters and plotted against the average g-factor, max g-factor, and RMSE, to try to find a correlation between the Spread out Range and the quality of the reconstructed image.

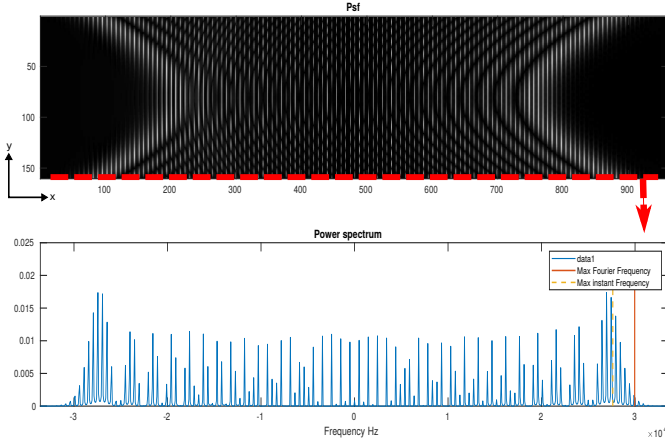


Figure 4.10: Point Spread Function and its power spectrum. Top: PSF in image space and bottom: power spectrum of the first line of PSF (marked with red). The maximum instantaneous frequency approximates the max Fourier frequency. The Spread-out range is twice the max instantaneous frequency.

4.2.2. NUMBER OF SINE CYCLES EFFECT

From equations 4.8-4.10 it can be inferred that higher gradient amplitudes G_y and G_z would produce a larger Range of Spread, but it is not clear what the effect of number of sine cycles is. To find that out, Point Spread Functions when varying the number of sines and keeping the other parameters fixed were simulated. With the higher Slew Rate of the insert gradient coil, it is possible to apply a higher number of sine cycles in the z direction. The effect of applying a different combination of sine cycles in the y and z direction was as well investigated.

4.2.3. PIXEL BANDWIDTH EFFECT

The pixel bandwidth affects the scan time, as it can be seen from the following equation, the readout time is inversely proportional to the pixel bandwidth p_{bw} :

$$t_r = \frac{1}{p_{bw}} \quad (4.11)$$

So in general a larger pixel bandwidth will allow for a shorter readout time, which could shorten the total scan time. The relation between p_{bw} and quality of image was as well investigated.

To further investigate the effect of the Wave-CAIPI parameters, the following empirically selected parameter combinations were tested: low, mid, high and very high gradient amplitude and pixel Bandwidth, table 4.3.

Parameter	Values			
	Low	Mid	High	Very High
Gy (mT/m)	6	10	20	30
Gz (mT/m)	6	30	50	70
Sinsy (cycles)	7	8	4	2
Sinsz (cycles)	7	14	21	28
p_{bw} (Hz)	70	150	300	600

Table 4.3: Parameter configurations for further analysis

4.2.4. TIME GAIN, CONVENTIONAL GRADIENT VS INSERT GRADIENT

An analysis of different parameters was conducted to compare the possible time gain when using the insert gradient coil compared to conventional coils. As previously stated, one of the main characteristics of the insert gradient coil is that allows to apply a higher amplitude and number of sines.

To prove that the same spread out range, calculated with equation 4.8 can be achieved in a shorter time when using the insert coil compared with a conventional one, firstly the range of spread was calculated for different Wave-CAIPI parameters combination for both type of gradients. Secondly the g-average, g-max and RMSE were calculated for parameter combinations. Lastly the time needed to generate that combination of gradient amplitude and number of sines was calculated using the following equation:

$$t = 4R_t Sins \quad (4.12)$$

Where $Sins$ is the number of cycles and R_t is the raise time given by:

$$R_t = \frac{G}{SR} \quad (4.13)$$

To better understand equation 4.12 a diagram of the sine gradient form can be found in figure 4.11.

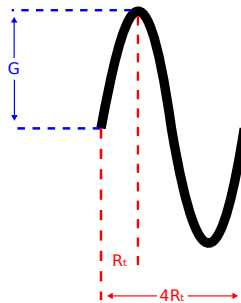


Figure 4.11: Sine wave gradient diagram, maximum gradient amplitude G and rise time R_t , one sine cycle is four times the R_t

4.3. IMPLEMENTATION IN SCANNER

To be able to test the Wave-CAIPI strategy, a sequence was programmed into the 7 Tesla scanner at the UMC Utrecht to test the results from the simulations. A gradient-echo sequence was modified to play sinusoidal gradients in the phase y and partition z encoding during readout. To do so, the source code of the scan was modified and five new parameters were added:

1. *Wave CAIPI* : parameter to activate Wave-CAIPI acquisition
2. *WC Phase strength*: Amplitude of the phase encoding gradient
3. *WC Phase periods*: Number of cycles phase encoding gradient
4. *WC Slice strength*: Amplitude of the slice encoding gradient
5. *WC Slice periods*: Number of cycles slice encoding gradient

These new parameters in the scanner environment can be found in figure 4.12

Summary	Geometry	Contrast	Motion	Dyn/Ang	Postp
Recon voxel size (mm)		1			
Fold-over suppression		no			
Slice oversampling		default			
RF select. FOS		no			
Reconstruction matrix		448			
SENSE		no			
+Wave CAIPI		yes			
+WC Phase strength		6			
+WC Slice strength		6			
+WC Phase periods		7			
+WC Slice periods		7			
k-tBLAST		no			
Overcontiguous slices		no			
Stacks		1			

Figure 4.12: Parameters added to the scanner environment

A new function to create the sine waves was also added to the source code. To create the cosine wave, the gradient has to be ramped-up before the read-out, the ramp-up time is calculated with the following formula:

$$ramp = \frac{GzGr_{dwell}}{SR} \quad (4.14)$$

Where Gz is the gradient amplitude in the slice direction, Gr_{dwell} is the gradient dwell time (time between samples) and SR is the gradient maximum slew rate. A visual representation of the sequence diagram, can be plotted directly from the scan environment, as it can be seen in figure 4.13.

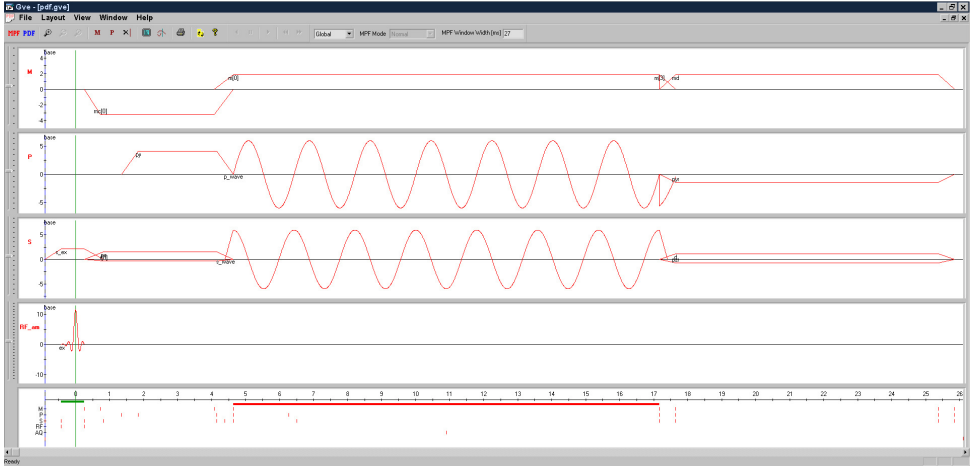


Figure 4.13: Wave-CAIPI sequence diagram, imported from scanner environment

4.3.1. IMAGING EXPERIMENTS AND RECONSTRUCTION

After the sequence was programmed into the scanner, the results from the original Wave-CAIPI paper [3] were replicated to prove that the implementation was successful. A phantom and a healthy volunteer were scanned. The parameters for both data sets were the following: FOV = $224 \times 224 \times 120 \text{ mm}^3$; voxel size = $1 \times 1 \times 2 \text{ mm}^3$; 32 receiver coils; maximum wave gradient amplitude = 6 mT/m; maximum slew rate = 21 T/m/s, using 7 sinusoidal wave cycles/readout. The scan time was 6 min with TR/TE = 27/10.9 ms and bandwidth = 80 Hz/pixel.

The scan protocol consisted of 6 different scans:

1. *Coil Sensitivity*: Scan to acquire the coil sensitivity map.
2. *Reference Point Spread Function Y*: Single slice projection scan in phase direction without applying sinusoidal gradients
3. *Point Spread Function Y*: Single slice scan in phase direction, applying sinusoidal gradient in phase direction
4. *Reference Point Spread Function Z*: Single slice projection scan in slice direction without applying sinusoidal gradients
5. *Point Spread Function Z*: Single slice scan in slice direction, applying sinusoidal gradient in slice direction
6. *Wave-CAIPI scan*: Fully sampled scan, applying sinusoidal gradients in phase and slice direction

To characterize the phase deposition from the sinusoidal gradients, the phase of the Reference Point Spread Function scans (2 and 4) was subtracted from the the phase of the Point Spread function scans (3 and 5) respectively. The result was interpolated to

cover all the desired FOV. Lastly, PSF Y and PSF Z are combined to arrive at the final 3D Point Spread Function that characterizes the phase deposited by the wave gradients, this process can be seen in figure 4.14.

To arrive at the under-sampled Wave-CAIPI image, the raw K-space data from the fully sampled scan (6) is multiplied by a 2D CAIPI mask, a 3D FFT is then applied to the resulted matrix. The data matrix is further cropped to the reduced FOV due to under-sampling, arriving to the final Wave-CAIPI image as it can be seen in figure 4.15.

After obtaining the Coil Sensitivity map, Point Spread Function, and Wave-CAIPI image, the underlying magnetization can be obtained, iteratively solving the linear system of equations in 3.7. The same algorithm used for the simulations was used to reconstruct the retrospectively under-sampled data from the scanner.

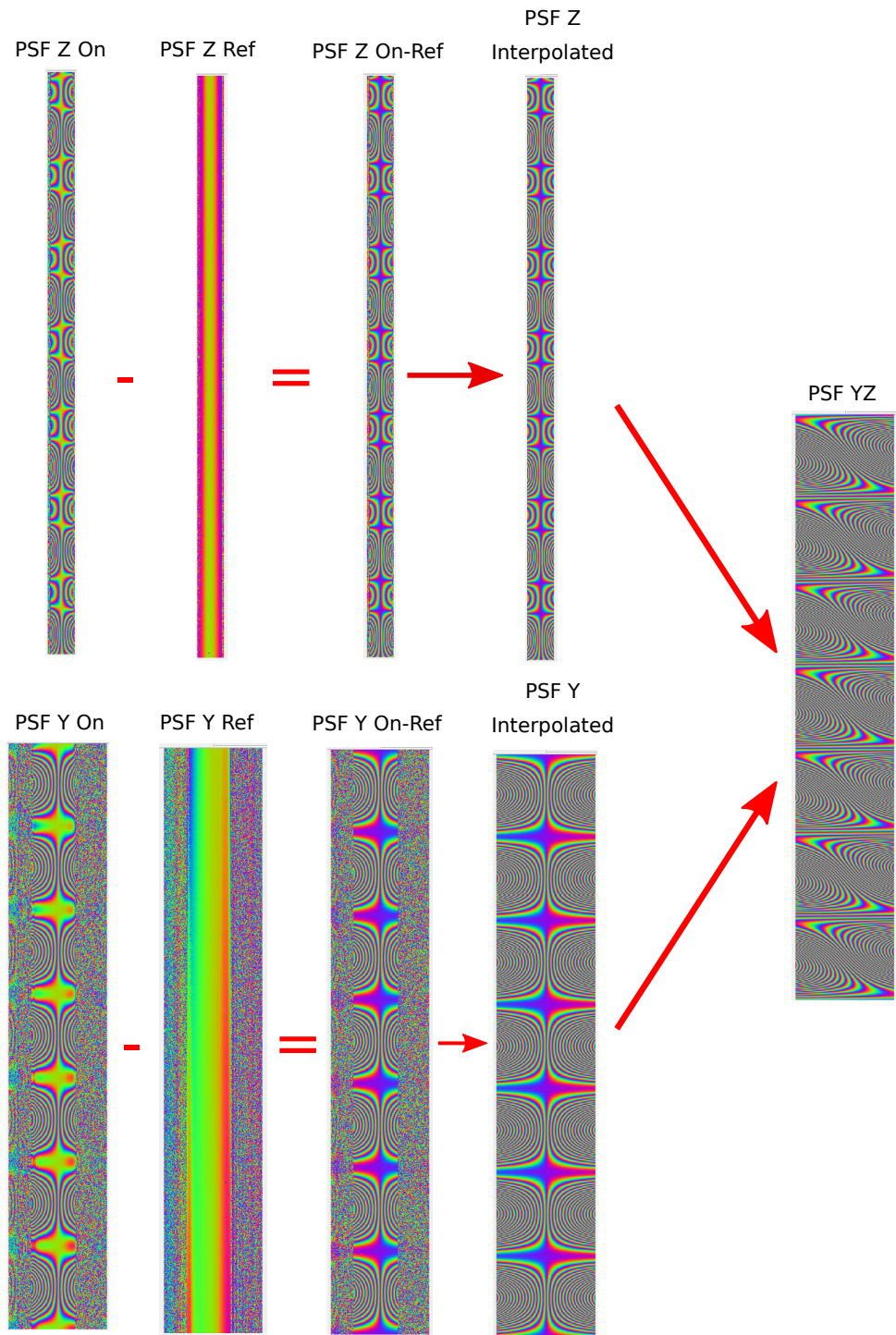


Figure 4.14: Point Spread Function from scanner. The phase of the PSF with sine gradients off (PSF Ref) is subtracted from PSF when gradients on (PSF On), the data is then interpolated to cover the full FOV. Phase and slice PSFs are further combined into PSF YZ

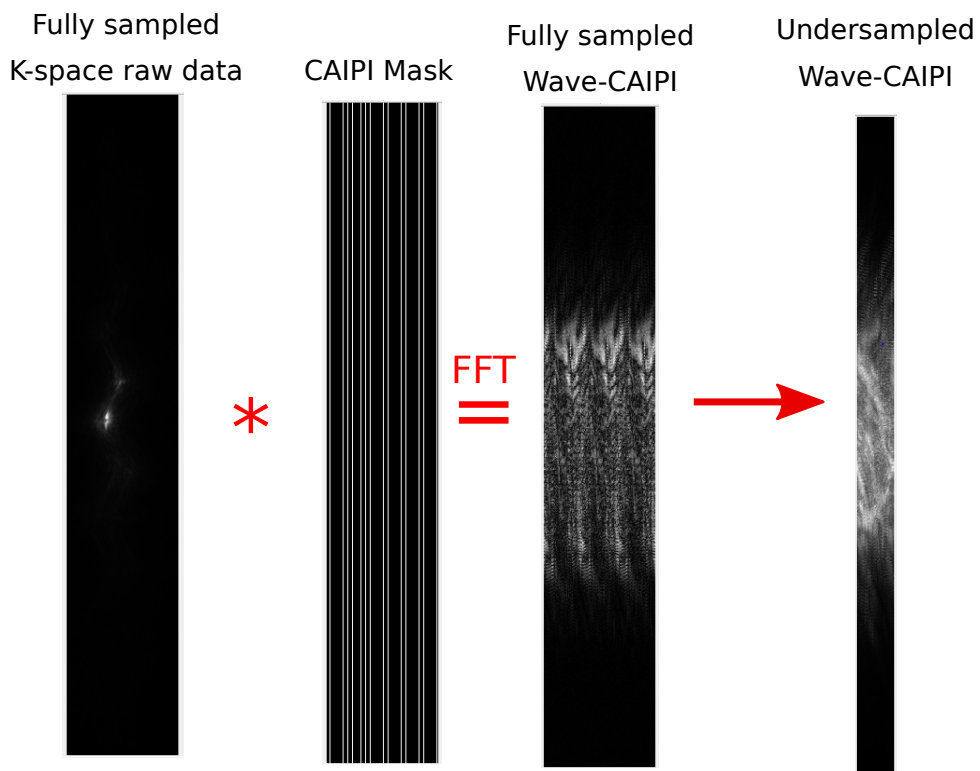


Figure 4.15: Under-sampling Wave-CAIPI from scanner. The fully sampled K-space data from the scanner is multiplied with a mask in a 2D CAIPI pattern, after a FFT, the fully sampled Wave-CAIPI image is cropped to arrive at the under-sampled Wave-CAIPI image

5

RESULTS

As previously mentioned, the goal of this project was to find out how can Wave-CAIPI together with a high efficiency insert gradient coil reduce the MRI imaging time. To do so, extensive simulations and in-vivo experiments were performed as described in section 4. This chapter presents the results obtained from this work.

5.1. SIMULATIONS

To test the effect of different Wave-CAIPI parameters in the image reconstruction, the steps used to obtain the simulated image were followed. Two different under-sampling factors ($R=3 \times 3$ and $R=4 \times 4$) were tested. This tests used simulated Point Spread Function for the phantom and brain images. Examples of this reconstructions and its g-factor map can be found in figures 5.1 and 5.2.

Phantom reconstruction for a matrix size $160 \times 160 \times 80$, under-sampling of $R=4 \times 4$, Low Wave-CAIPI parameters $G_y = 6 \text{ mT/m}$, $G_z = 6 \text{ mT/m}$, $S_{\text{insy}} = 7 \text{ cycles}$, $S_{\text{insz}} = 7 \text{ cycles}$ and Pixel Bandwidth = 70 Hz:

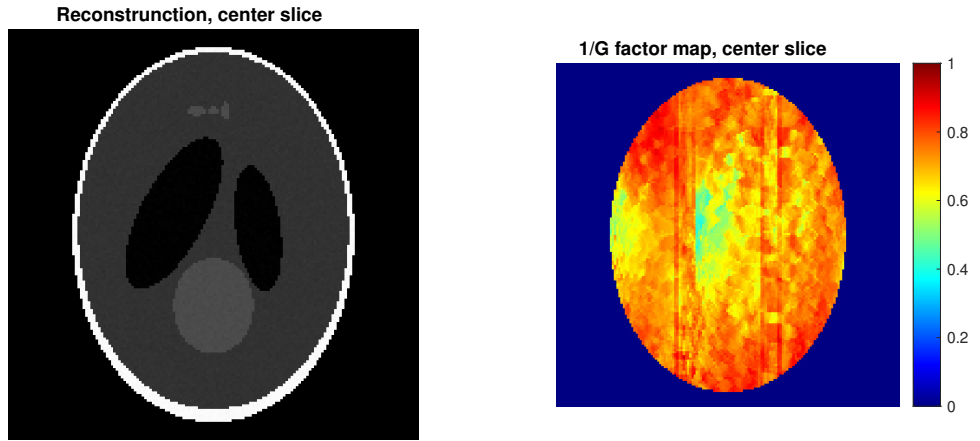


Figure 5.1: Phantom Wave-CAIPI reconstruction, $R=4 \times 4$ under-sampling factor

Brain reconstruction for a matrix size $224 \times 224 \times 60$, under-sampling of $R=3 \times 3$, Low Wave-CAIPI parameters $G_y = 6 \text{ mT/m}$, $G_z = 6 \text{ mT/m}$, $S_{\text{insy}} = 7 \text{ cycles}$, $S_{\text{insz}} = 7 \text{ cycles}$ and Pixel Bandwidth = 70 Hz:

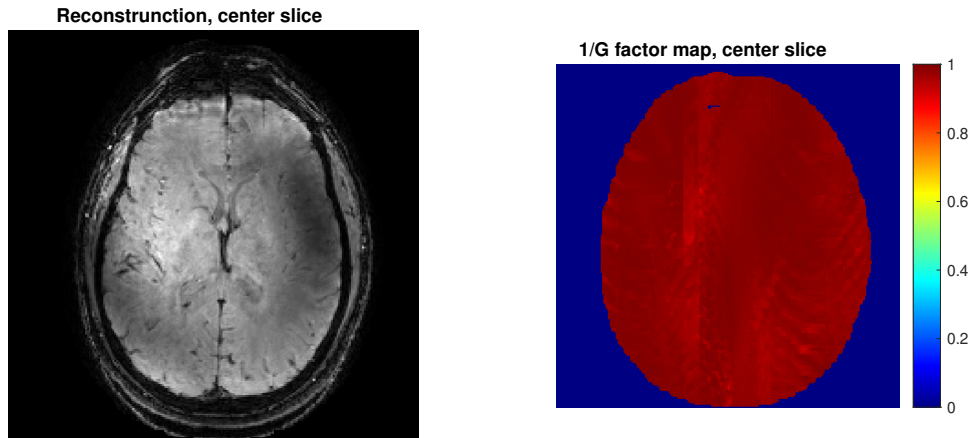


Figure 5.2: Brain Wave-CAIPI reconstruction, $R=3 \times 3$ under-sampling factor

5.2. PARAMETERS OPTIMIZATION

5.2.1. RANGE OF SPREAD EFFECT

Figures 5.3, 5.4 and 5.5 show the relation between the spread out range, equation 4.8, and the three different quality measurements, equations 3.10-3.12, for different Wave-CAIPI parameters, FOV and under-sampling factors. As it can be seen from the left and center plots, the RMSE and G-average follow a L shape curve. It can be seen that the higher the range of spread, the smaller the g-factor penalty and Root Mean Squared Error.

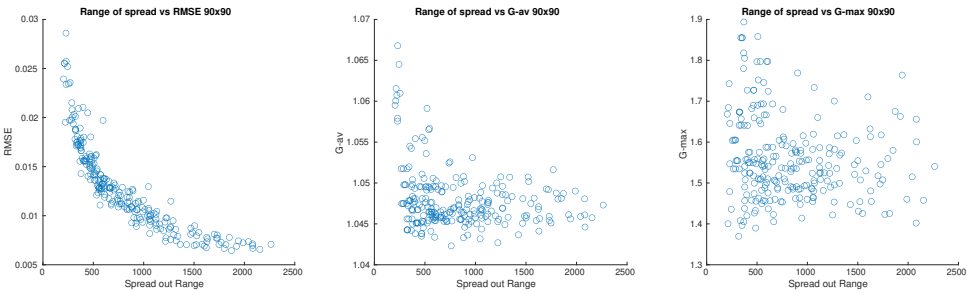


Figure 5.3: Range of Spread vs RMSE, G-av and G-max, for a matrix size of 90x90x90 and under-sampling factor $R=3 \times 3$, different Wave-CAIPI parameters

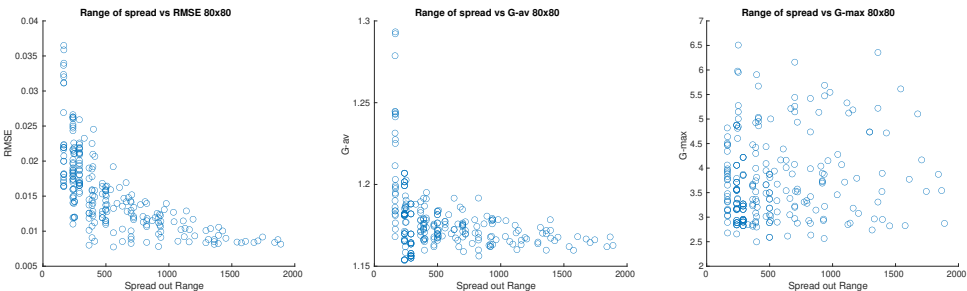


Figure 5.4: Range of Spread vs RMSE, G-av and G-max, for a matrix size of 80x80x80 and under-sampling factor $R=4 \times 4$, different Wave-CAIPI parameters

No correlation was found between the range of spread and the maximum g-factor, as seen in the right-most figures of 5.3, 5.4 and 5.5. To investigate this, the g-factor values for different parameter combinations were plotted and it was found that there are a few high values in the calculated g-factor data as shown in figure 5.6. This could be caused by the Coil Sensitivities or the method used to calculate the g-factor map.

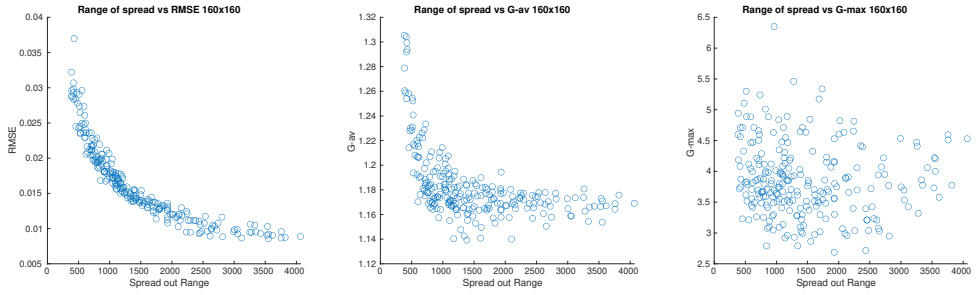


Figure 5.5: Range of Spread vs RMSE, G-av and G-max, for a matrix size of 160x160x160 and under-sampling factor $R=4 \times 4$, different Wave-CAIPI parameters

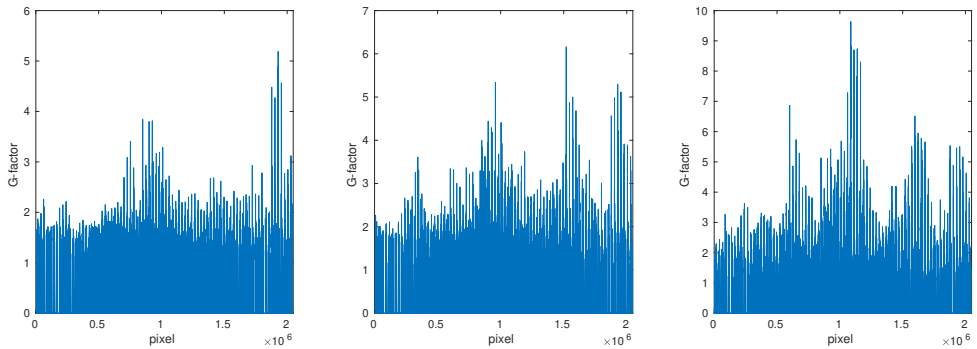


Figure 5.6: G-factor values for all pixels of matrix size 160x160x80, under-sampling $R=4 \times 4$, $G_y = 6$ mT/m, $G_z = 6$ mT/m, $S_{insy} = 7$ cycles, $S_{insz} = 7$ cycles. Left: $p_{bw} = 70$, Center: $p_{bw} = 150$ and Right: $p_{bw} = 300$. Only few high g-factor values are present.

As stated in section 4.1.1, an image of a fully-sampled brain was as well used to investigate the effect of the different parameters. It was found that using a Very High Wave-CAIPI parameters combination ($G_y = 30$ mT/m, $G_z = 70$ mT/m, $S_{\text{insy}} = 2$ cycles, $S_{\text{insz}} = 28$ cycles) significantly improves the reconstruction, the RMSE is four times lower with very high parameters compared with low ones, as it can be seen in the following figure:

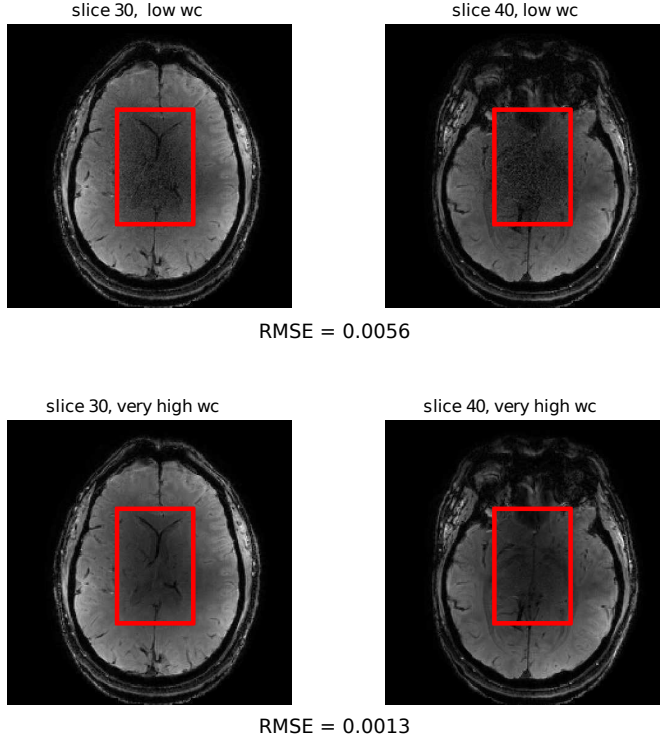


Figure 5.7: Brain reconstruction pixel BW = 70, R=4x4. Top row: Low Wave-CAIPI parameters $G_y = 6$ mT/m, $G_z = 6$ mT/m, $S_{\text{insy}} = 7$ cycles, $S_{\text{insz}} = 7$ cycles. Bottom row: Very High Wave-CAIPI parameters $G_y = 30$ mT/m, $G_z = 70$ mT/m, $S_{\text{insy}} = 2$ cycles, $S_{\text{insz}} = 28$ cycles. The RMSE is four times lower when using very high parameters.

5.2.2. NUMBER OF SINE CYCLES EFFECT

From the previous section we found that a larger range of spread produces better reconstructions, from equation 4.8 we know that larger gradient amplitudes increases the range of spread. Nevertheless, no conclusions have been obtained on the effect of the number of sines in the quality of the image.

The results of the simulations to find out the effect of the number of sine cycles can be found in table 5.1. It shows that higher number of cycles reduces the RMSE but does not significantly change the G-average. Figures 5.8 - 5.10 show the Point Spread Function and the power spectrum of the first readout line (horizontal axis). Each PSF vertical line represents a copy with different intensity of the original under-laying image (spread out)

so the distance between each line affects the spreading and can contribute to a better reconstruction.

As it can be seen in figures 5.8 and 5.10, higher number of sine cycles increases the distance between frequency lines in the PSF and playing different number of cycles in the y and z direction spreads more the frequency content as seen in figure 5.9, this could have a negative impact in the reconstruction since the content (more vertical lines are present) of each pixel is distributed in more frequencies and could be difficult to identify them from noise. We conclude that it is better to apply a high number of sines and the same number for the phase y and slice z directions.

Gy (mT/m)	Gz (mT/m)	Sinsy (cycles)	Sinsz (cycles)	p_{bw} (Hz)	G-av	RMSE
6	6	7	7	70	1.74	0.0996
6	6	7	20	70	1.92	0.0965
6	6	20	20	70	1.86	0.0906

Table 5.1: Number of sines analysis, G-av and RMSE for three different combinations of Sinsy and Sinsz

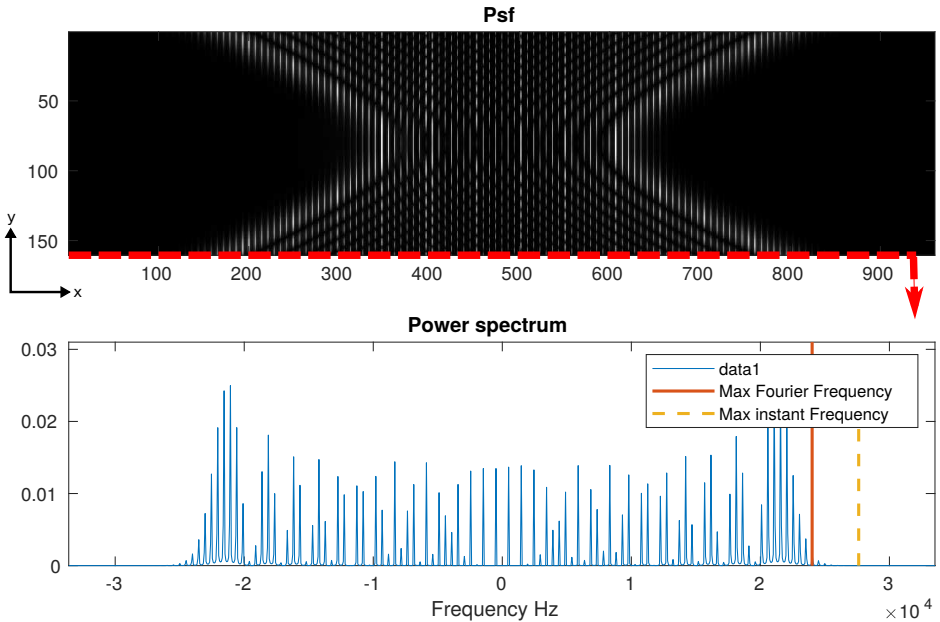


Figure 5.8: Point Spread Function, Sinsy = 7 and Sinsz = 7. Top: PSF in image space and bottom: power spectrum of the first line of PSF (marked with red). Each frequency has relatively high content as seen from the limits of the y axis.

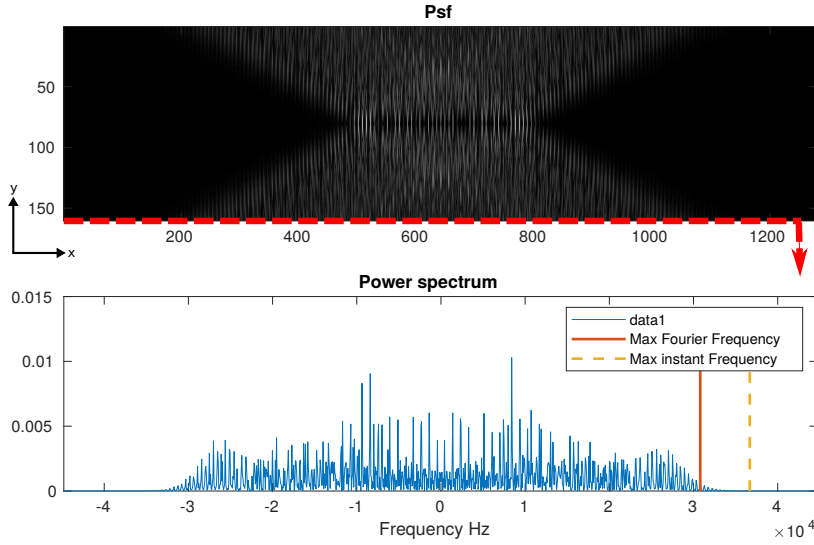


Figure 5.9: Point Spread Function, Sinsy = 7 and Sinsz = 20. Top: PSF in image space and bottom: power spectrum of the first line of PSF (marked with red). When using different number of sines in y and z direction, the signal power is distributed into more frequencies with low content as seen from the limits of the y axis.

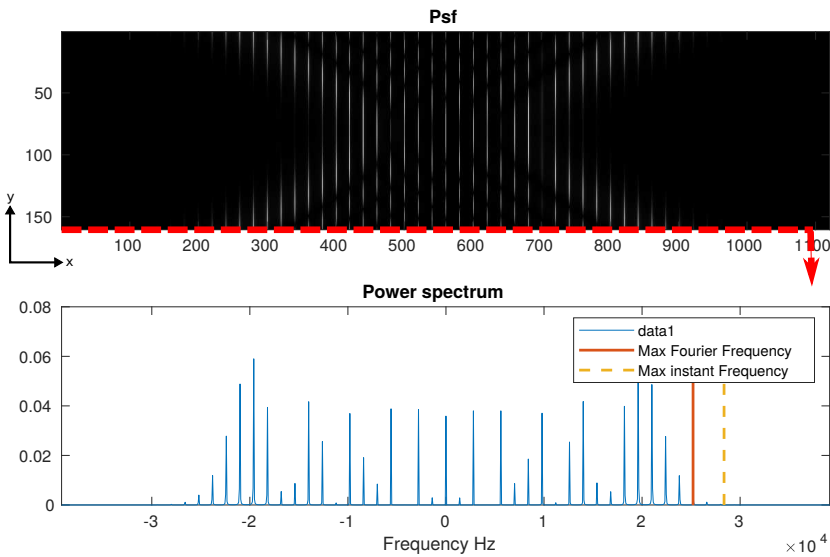


Figure 5.10: Point Spread Function, Sinsy = 20 and Sinsz = 20. Top: PSF in image space and bottom: power spectrum of the first line of PSF (marked with red). When using a large number of sines in y and z direction, the signal power is distributed into less frequencies with high content as seen from the limits of the y axis.

5.2.3. PIXEL BANDWIDTH EFFECT

After the findings of the previous section, the effect of the pixel bandwidth was investigated. As it can be seen in plot 5.11 and figures 5.12, 5.13, larger pixel bandwidths produce worse reconstructions. As induced from equation 4.8, larger pixel bandwidth will produce smaller spread out range and thus higher g-factor and worse reconstruction. Using the insert gradient coil allows us to use a higher gradient amplitude and number of sines. Subsection 4.2.4 investigates if increasing the amplitude and number of sines can generate a similar reconstruction with higher pixel bandwidth (shorter readout time).

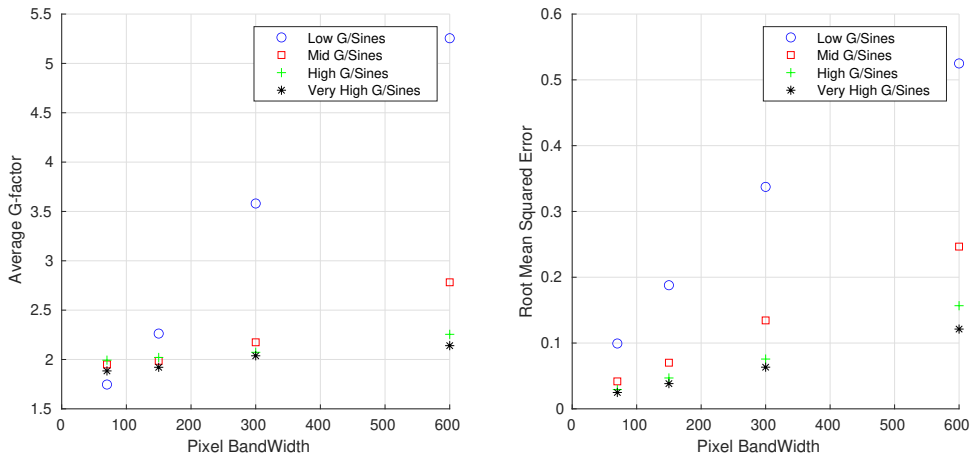


Figure 5.11: Pixel Bandwidth analysis, different pixel bandwidth sizes vs average g-factor and RMSE. Larger pixel BW produces worse average G-factor and therefore worse reconstruction

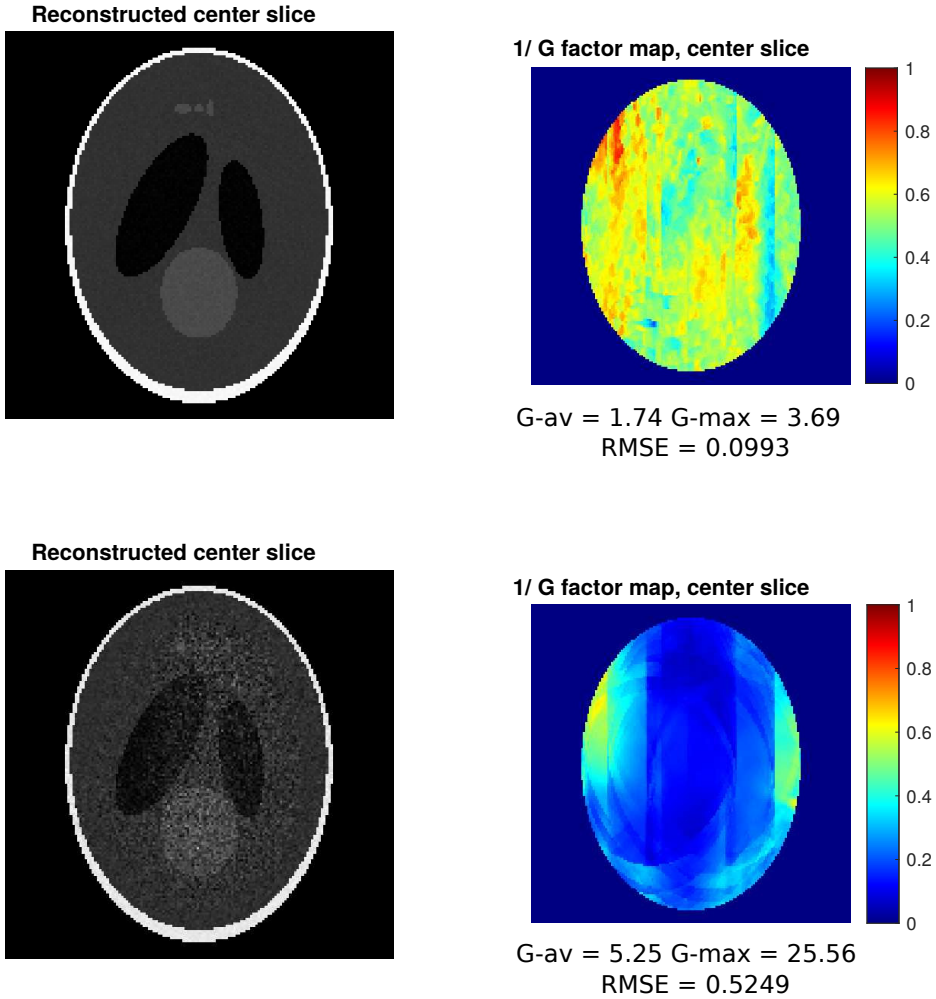


Figure 5.12: Low Wave-CAIPI parameters, $G_y = 6 \text{ mT/m}$, $G_z = 6 \text{ mT/m}$, $\text{Sinsy} = 7 \text{ cycles}$, $\text{Sinsz} = 7 \text{ cycles}$. Top row: 70 Hz pixel BW. Bottom row: 600 Hz pixel BW. Larger pixel BW produces worse reconstruction

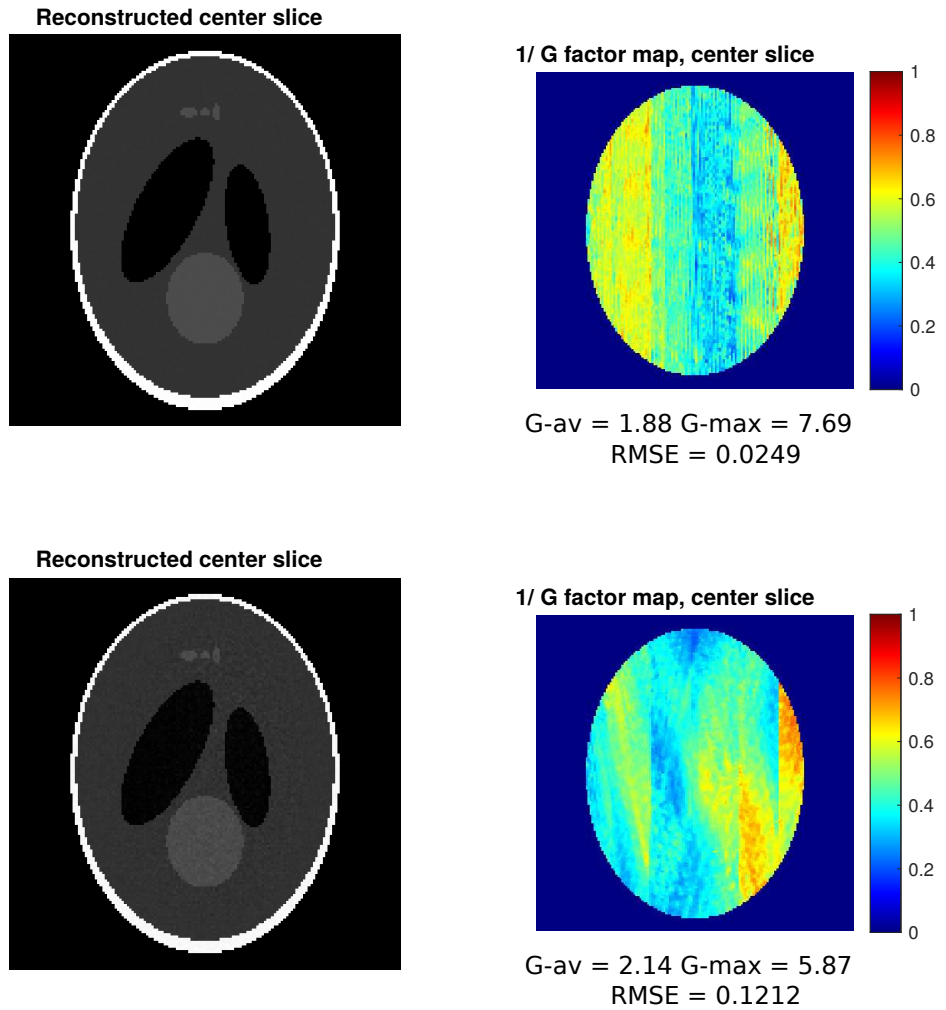


Figure 5.13: Very High Wave-CAIPI parameters, $G_y = 30$ mT/m, $G_z = 70$ mT/m, $S_{\text{insy}} = 2$ cycles, $S_{\text{insz}} = 28$ cycles. Top row: 70 Hz pixel BW. Bottom row: 600 Hz pixel BW. Larger pixel BW produces worse reconstruction

5.2.4. TIME GAIN, CONVENTIONAL GRADIENT VS INSERT GRADIENT

From the past sections, we know that larger spread out range produces better reconstructions. We also know that increasing the gradient amplitudes produces a larger spread out range, on the other hand increasing the pixel bandwidth would have the opposite effect. Equation 4.11 suggests that using larger pixel BW could reduce total imaging time. In general, we would like to use larger pixel bandwidth without affecting the range of spread, this might be possible with the insert gradient coil, the results of this analysis are presented in this section.

Tables 5.2-5.4 and figures 5.14- 5.16 show results of reconstructions for a 160x160x80 matrix size and a under-sampling factor of $R=4 \times 4$. We can see that using the insert gradient coil a similar range of spread, average g-factor and Root Mean Squared Error can be achieved even if a higher pixel BW is used (shorter readout time). This is because the insert gradient coil allows us to use a higher gradient amplitude and play a higher number of sines in the z direction.

Gy (T/m)	Gz (T/m)	Sinsy (cycles)	Sinsz (cycles)	p_{bw} (Hz)	G-av	RMSE	Readout time (s)	Times faster
Conventional gradient system								
0.015	0.015	17	17	100	1.24	0.0481	0.0100	
Insert gradient system								
0.006	0.030	10	17	150	1.32	0.0460	0.0067	1.5
0.018	0.030	11	27	150	1.27	0.0426	0.0067	1.5
0.006	0.040	10	11	200	1.33	0.0482	0.0050	2
0.018	0.040	5	7	250	1.27	0.0524	0.0040	2.5
0.014	0.040	5	14	250	1.31	0.0494	0.0040	2.5
0.006	0.060	6	6	300	1.34	0.0511	0.0033	3
0.010	0.080	6	6	400	1.34	0.0511	0.0025	4

Table 5.2: Parameter combinations that yield a range of spread ~ 1500 , conventional vs insert gradient system. Reconstructions with a $R=4 \times 4$ acceleration factor. A speed up by a factor of 4 is possible with insert coil at a maximum Slew Rate of $\sim 1,200$

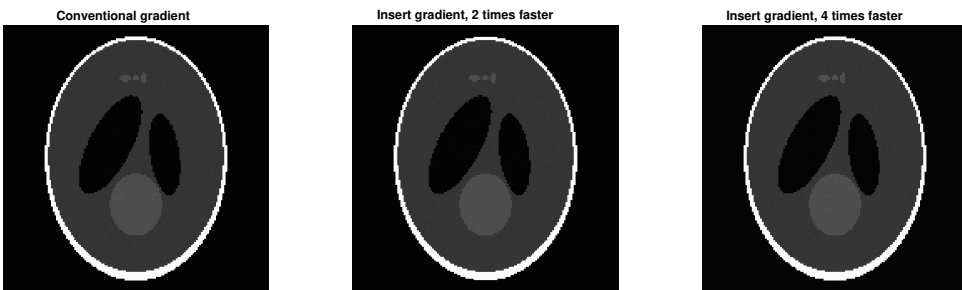


Figure 5.14: Under-sampling factor $R=4 \times 4$, range of spread ~ 1500 . Reconstructions of conventional gradient vs insert gradient. Left: conventional gradient system (row 1) parameters, center: insert gradient (row 3) parameters, right: insert gradient (last row) parameters. The quality of all three reconstructions is similar

Gy (T/m)	Gz (T/m)	Sinsy (cycles)	Sinsz (cycles)	p_{bw} (Hz)	G-av	RMSE	Readout time (s)	Times faster
Conventional gradient system								
0.019	0.019	3	3	50	1.25	0.0319	0.0200	
Insert gradient system								
0.010	0.050	7	7	100	1.26	0.0320	0.0100	2
0.022	0.030	5	18	100	1.28	0.0321	0.0100	2
0.026	0.060	8	6	150	1.24	0.0320	0.0067	3
0.006	0.070	5	13	150	1.32	0.0319	0.0067	3
0.006	0.100	12	6	200	1.32	0.0319	0.0050	4
0.014	0.120	8	5	250	1.31	0.0320	0.0040	5

Table 5.3: Parameter combinations that yield a range of spread ~ 3500 . Reconstructions of conventional vs insert gradient system. Reconstructions with a R=4x4 acceleration factor. A speed up by a factor of 5 is possible with the insert coil at a maximum Slew Rate of ~ 940

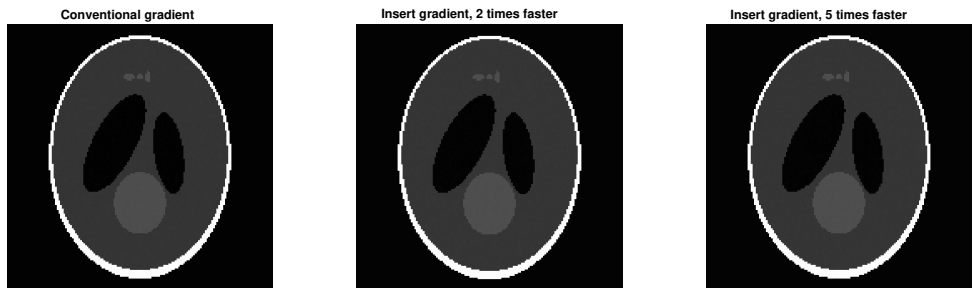


Figure 5.15: Under-sampling factor R=4x4, range of spread ~ 3500 . Reconstructions, conventional gradient vs insert gradient. Left: conventional gradient system (row 1) parameters, center: insert gradient (last row), right: insert gradient (row 7). The quality of all three reconstructions is similar

Gy (T/m)	Gz (T/m)	Sinsy (cycles)	Sinsz (cycles)	p_{bw} (Hz)	G-av	RMSE	Readout time (s)	Times faster
Conventional gradient system								
0.037	0.037	15	15	50	1.23	0.0224	0.0200	
Insert gradient system								
0.010	0.100	11	8	100	1.31	0.0224	0.0100	2
0.030	0.090	7	13	100	1.26	0.0220	0.0100	2
0.014	0.110	12	13	100	1.32	0.0217	0.0100	2
0.006	0.100	12	18	100	1.34	0.0224	0.0100	2

Table 5.4: Parameter combinations that yield a range of spread ~ 7000 . Reconstructions of conventional vs insert gradient system. A speed up by a factor of 2 is possible with insert coil at a maximum Slew Rate of $\sim 1,130$

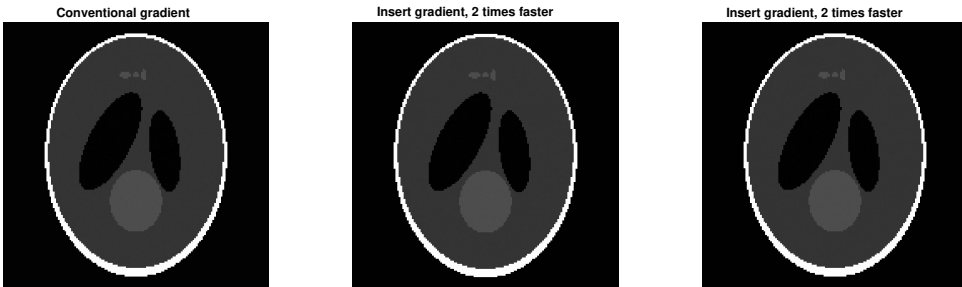


Figure 5.16: Under-sampling factor $R=4 \times 4$, range of spread ~ 7000 . Reconstructions conventional gradient vs insert gradient. Left: conventional gradient system (row 1) parameters, center: insert gradient (row 1) parameters, right: insert gradient (row 2) parameters. The quality of all three reconstructions is similar

5.3. IMPLEMENTATION IN SCANNER

5.3.1. IMAGING EXPERIMENTS AND RECONSTRUCTION

The steps described in section 4.3.1 were followed to reconstruct the retrospectively under-sampled Wave-CAIPI image acquired from the scanner. Figures 5.17 - 5.20 show the 224x224x60 reconstructed image when different under-sampling values are used.

We can see that the quality of the R=3x3 under-sampled reconstruction (figure 5.19) is similar to the one of the original published paper [3], this shows that the scanner implementation and reconstruction algorithm work as expected. The quality of the R=4x4 under-sampled reconstruction (figure 5.20) is not good when using the conventional gradient system, but as figure 5.7 shows using higher gradient amplitudes and number of sines would produce a better reconstruction.

Under-sampling factor of R=1x1:

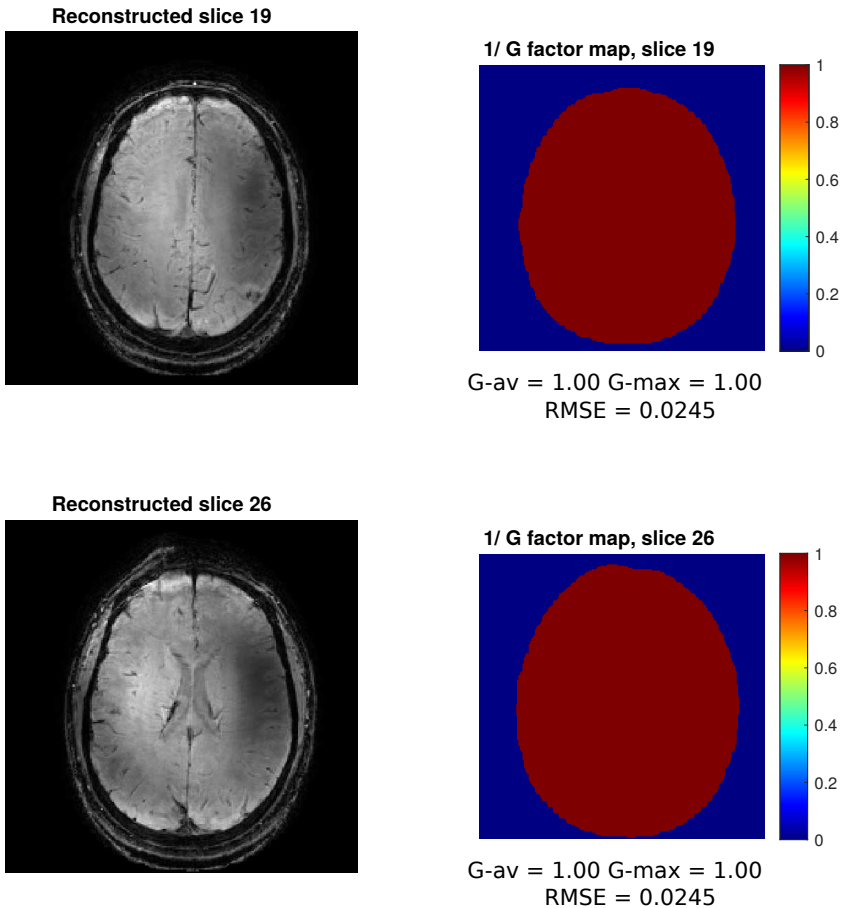


Figure 5.17: Baseline scanner Wave-CAIPI reconstruction, R=1x1 under-sampling factor

Under-sampling factor of $R=2 \times 2$:

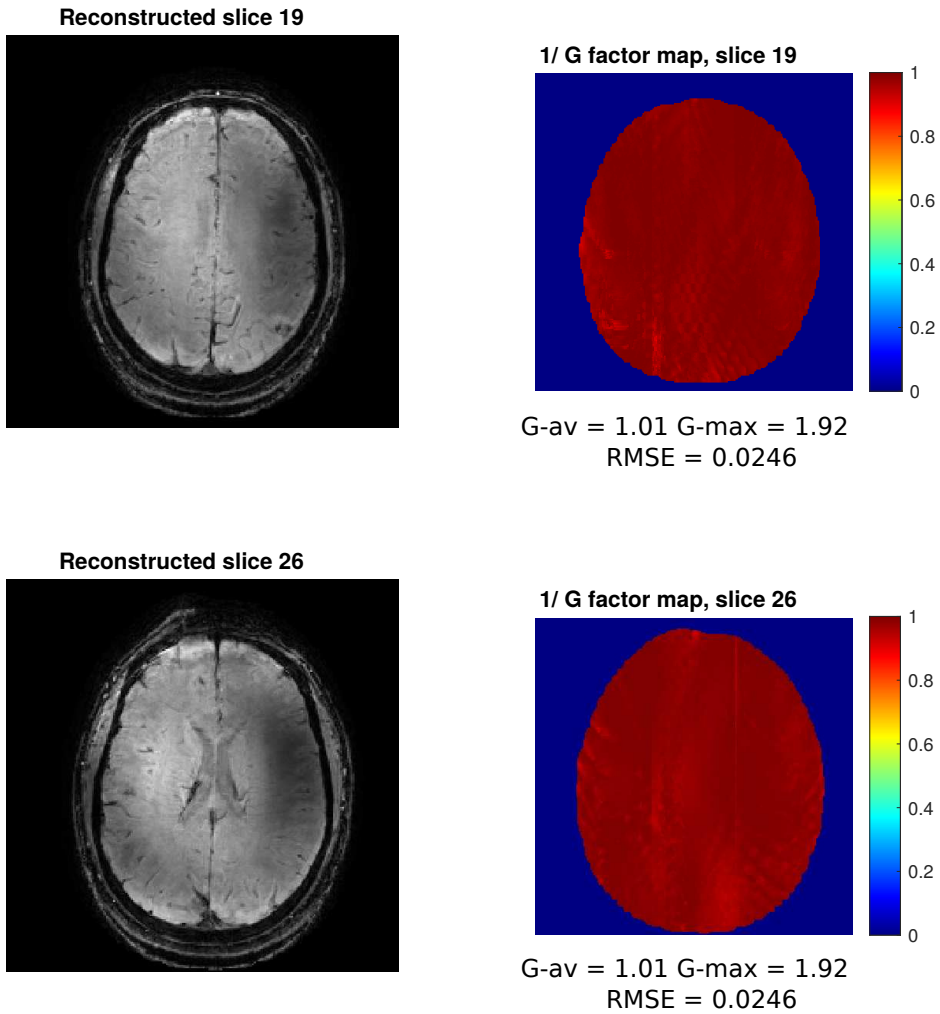


Figure 5.18: Scanner wave-CAIPI reconstruction, $R=2 \times 2$ under-sampling factor, g-average close to unity and very good reconstruction

Under-sampling factor of $R=3 \times 3$:

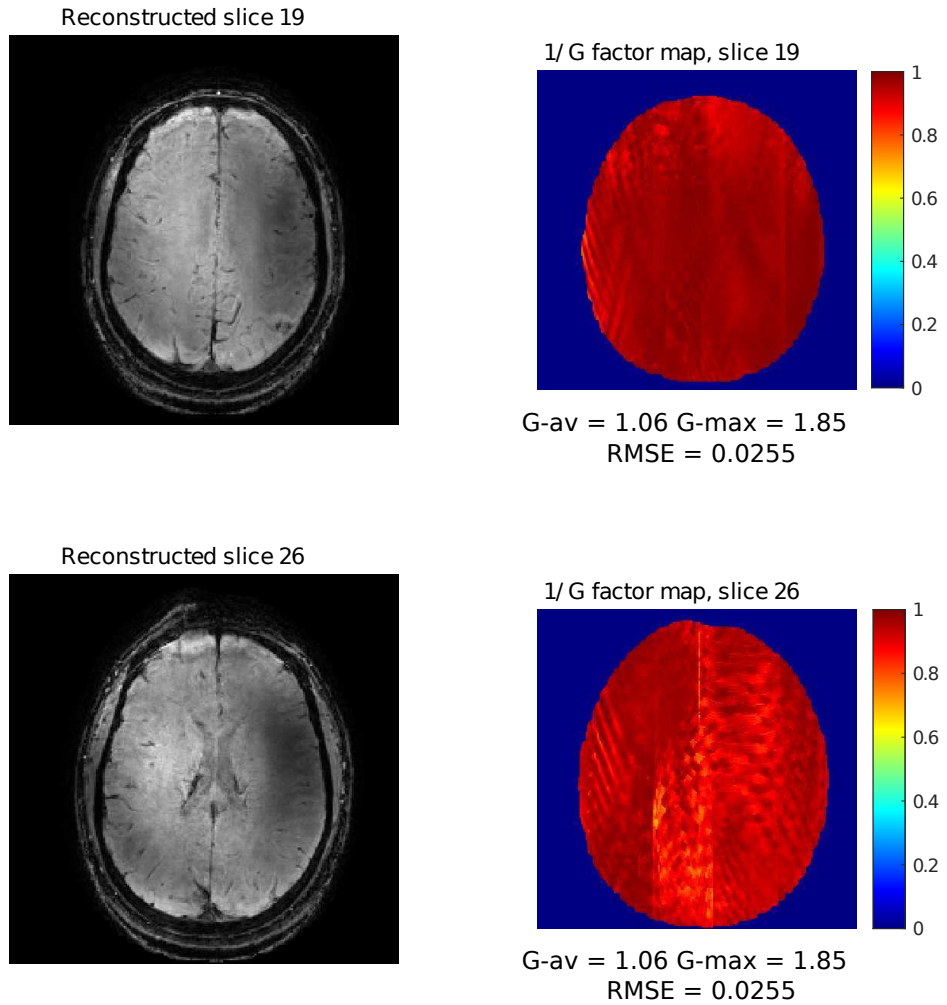


Figure 5.19: Scanner Wave-CAIPI reconstruction, $R=3 \times 3$ under-sampling factor, g-average close to unity and very good reconstruction, similar as original Wave-CAIPI paper [3]

Under-sampling factor of $R=4 \times 4$:

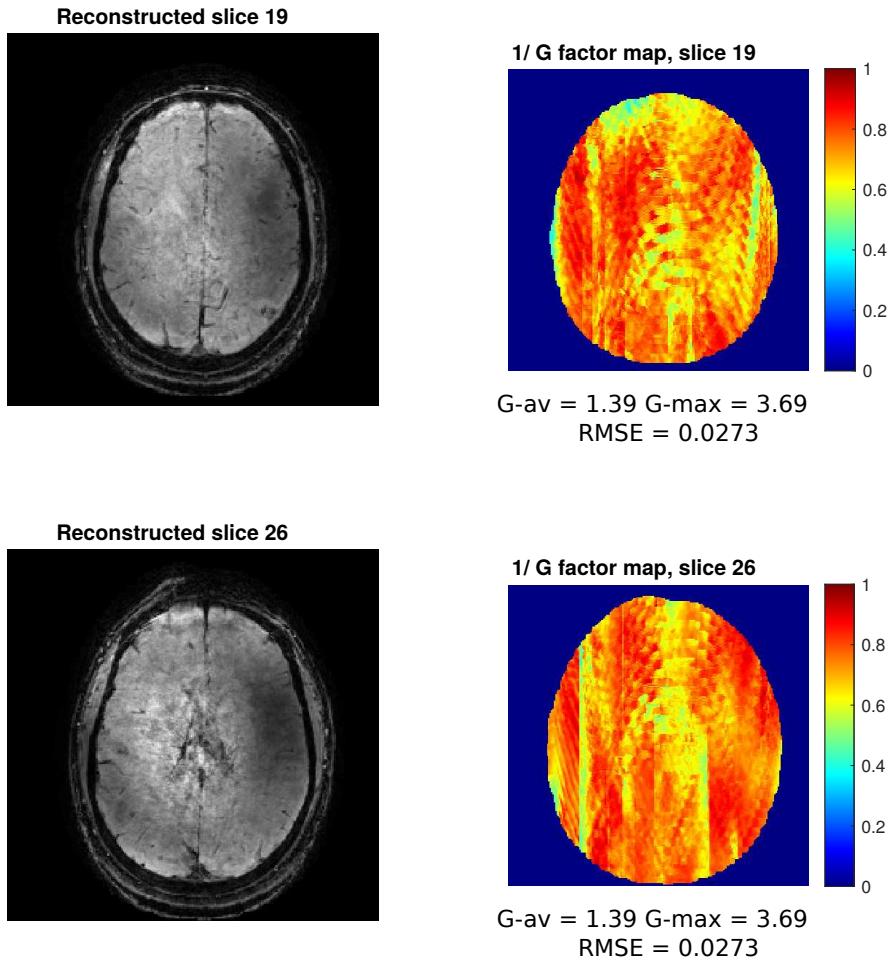


Figure 5.20: Scanner Wave-CAIPI reconstruction, $R=4 \times 4$ under-sampling factor, g-average outside accepted values (1-1.20) and bad reconstruction, according to simulations in figure 5.7, a significant better reconstruction can be achieved when using higher gradient amplitude and number of sine cycles

6

DISCUSSION, CONCLUSIONS, LIMITATIONS AND FURTHER WORK

This work has investigated the effect that the different Wave-CAIPI parameters 3.1 have in the quality of the reconstructed image. To do so, their effect was investigated separately with simulations. Two analysis were performed to characterize the possible imaging time reduction. Firstly, the maximum under-sampling factor that produces a good quality image was investigated for an R=4x4 under-sampling factor. Secondly, the decrease in acquisitions time that can be obtained using the described insert gradient coil was explored.

From the simulations performed with different Wave-CAIPI parameter configurations in sections 5.2.1 and 5.2.2, it can be concluded that the spread out range increases when higher gradient amplitudes and number of sines are applied during readout, and this in turn improves the overall quality of the reconstructed image. From section 5.2.3 it can also be concluded that larger pixel bandwidth produces worse reconstructions, this can be explained in two different ways, the first one because the larger the pixel bandwidth, the shorter the range of spread as in can be seen from equation 4.8. The other explanation is that when more spatial frequencies are sampled the Signal to Noise Ratio is decreased, the signal power in each frequency is smaller and thus it can be difficult to separate it from the noise.

From section 5.2.4, it can be concluded that using the high efficiency insert gradient coil allows to achieve the same spread out range even when higher pixel bandwidth are used (shorter read-out time). The time gain can be up to five times faster compared with conventional gradient coil systems. This could allow to shorten the TE and TR of different sequences, but more work has to be done to make sure the desired contrast is obtained even with shorter Echo and Repetition times. For Echo Planar Imaging sequences, it can be especially useful since in these type of acquisitions, switching the gradient faster allows to excite more K-space lines in a shorter time, reducing the overall scan time, distortion and signal loss.

It has been shown in section 5.3.1 that the data acquired from the Wave-CAIPI implementation on the scanner can be reconstructed with the proposed algorithm. The reconstructed image for a reduction factor of $R=3 \times 3$ (figure 5.19) have similar quality as the work described in the original Wave-CAIPI paper [3], a possible difficulty when implementing this strategy is failing to properly characterize the Point Spread Function from the single slice projection data as explained in section 4.3.1, nevertheless, the proposed sequences and algorithms give positive results.

For high gradient amplitude and number of sines, a large oversampling factor in the readout direction is needed, in this case accurately obtaining the PSF from single slice projection scans could be a difficult task. For this reason, another approach investigated to obtain the PSF was to use a field camera [22] to measure the extra phase induced by the wave gradients, since this requires specialized equipment and better reconstructions with the tested set-up were not obtained with this approach, it was not included in this report.

In other works [20] [21] the main limitation to be able to achieve smaller g-factor and higher under-sampling factors is the maximum gradient amplitude that can be achieved with a conventional gradient system. This work addresses this limitation and presents the results when a high efficiency gradient insert coil capable of increasing the gradient strength of the z direction is used. As it can be seen in table 2.1 the maximum gradient amplitude of the insert gradient coil is up to 4 times higher than a conventional gradient coil. According to simulations, under-sampling factor of $R=4 \times 4$ with very high Wave-CAIPI parameters ($G_y = 30$ mT/m, $G_z = 70$ mT/m, $S_{in}y = 2$ cycles and $S_{in}z = 28$ cycles) and $p_{bw} = 70$ Hz, could produce an image with acceptable quality, implementation in the scanner is needed to assess whether or not that parameter combination produce images of good quality.

In summary, the best acquisition parameters are the ones with not only high gradient amplitudes but also with the same large number of sine cycles in phase y and partition z encoding directions. The ideal combination of parameters would possible allow a $R=4 \times 4$ under-sampling factor. Using the insert gradient coil could allow to shorten the read out time up to five times faster compared with conventional gradient systems, this could be useful for EPI sequences.

6.1. LIMITATIONS

One of the limitations of this work is that only the theoretical method to calculate the g-factor was used. Several methods have been proposed which could have slightly different g-factor results, such as the pseudo multiple replica [23], which is a robust technique but it is time consuming. Since the computation time of the pseudo multiple replica method is significantly longer than the theoretical one, it was decided not to use it in this project, further validation is advised to corroborate the implementation and results of the theoretical method. Nevertheless, the conclusions given in this report will still be valid with any other g-factor calculation method.

This project concludes that higher gradient amplitudes and number of cycles will produce a better reconstruction, but no parameter optimization framework has been included in this work, the tested configurations were empirically chosen and a better approach to select the optimal parameters could be developed, the paper by Polak [20]

does not use a parameter optimization, whereas the one from Wang [21] proposes a parameter optimization framework that could be adapted for the proposed configuration of this project.

6.2. FURTHER WORK

This project has proved with simulations that imaging reduction times are possible using the described insert gradient coil [2], it has also presented an image reconstruction algorithm. However, some work has to be done to further optimize the sequence parameters and to prove the results from simulations.

Expanding the optimization approach presented in [21] to work when more degrees of freedom are allowed, would allow us to make sure the best possible reconstruction is achieved. In terms of implementation in the scanner, the next steps are to implement the 2D CAIPI strategy into the scanner, this would allow to prospectively under-sample the data in a Wave-CAIPI manner to further reconstruct it with the proposed algorithm. In-vivo experiments using higher gradient amplitudes and number of sines have to be performed as well. A in depth analysis has to be carried out to evaluate whether the desired image contrast can be achieved if the TE/TR are shortened with the use of the insert gradient coil. Lastly, the Wave-CAIPI framework presented in this work can be modified for use with an EPI sequence to investigate the possible time reduction.

BIBLIOGRAPHY

- [1] W. A. Edelstein, M. Mahesh, and J. A. Carrino, *MRI: Time is dose - And money and versatility*, [Journal of the American College of Radiology](#) **7**, 650 (2010).
- [2] T. A. van der Velden, C. C. van Leeuwen, E. R. Huijting, M. Borgo, P. R. Luijten, D. W. Klomp, and J. C. Siero, *A lightweight gradient insert coil for high resolution brain imaging*, in *International Society of Magnetic Resonance in Medicine Honolulu* (2017) p. 4329.
- [3] B. Bilgic, B. A. Gagoski, S. F. Cauley, A. P. Fan, J. R. Polimeni, P. E. Grant, L. L. Wald, and K. Setsompop, *Wave-CAIPI for highly accelerated 3D imaging*, [Magnetic Resonance in Medicine](#) **73**, 2152 (2015).
- [4] E. Versteeg, D. Klomp, J. Hendrikse, and J. Siero, *Supersonic imaging with a silent gradient axis driven at 20 kHz*, [Proceedings of the 27th Annual Meeting of ISMRM](#) , #4586 (2019).
- [5] A. Hendrix, *Magnets, Spins, and Resonances An introduction to the basics of Magnetic Resonance*, [Siemens AG Medical Solutions](#) , 80 (2003).
- [6] H. Haynes and W. M. Holmes, *The emerging use of Magnetic Resonance Imaging (MRI) for 3D analysis of sediment structures and internal flow processes*, *Geomorphological Techniques* , 1 (2013).
- [7] C. E. Shannon, *Communication in the presence of noise*, [Proceedings of the IEEE](#) **86**, 447 (1998).
- [8] J. A. Fessler and B. P. Sutton, *Nonuniform fast Fourier transforms using min-max interpolation*, [IEEE Transactions on Signal Processing](#) **51**, 560 (2003).
- [9] A. Deshmane, V. Gulani, M. A. Griswold, and N. Seiberlich, *Parallel MR imaging*, [Journal of Magnetic Resonance Imaging](#) **36**, 55 (2012).
- [10] K. P. Pruessmann, M. Weiger, M. B. Scheidegger, and P. Boesiger, *SENSE: Sensitivity encoding for fast MRI*, [Magnetic Resonance in Medicine](#) **42**, 952 (1999).
- [11] M. A. Griswold, P. M. Jakob, R. M. Heidemann, M. Nittka, V. Jellus, J. Wang, B. Kiefer, and A. Haase, *Generalized Autocalibrating Partially Parallel Acquisitions (GRAPPA)*, [Magnetic Resonance in Medicine](#) **47**, 1202 (2002).
- [12] D. J. Larkman, *The g-Factor and Coil Design*, [Parallel Imaging in Clinical MR Applications](#) **3**, 37 (2007).
- [13] E. Kaza, U. Klose, and M. Lotze, *Comparison of a 32-channel with a 12-channel head coil: Are there relevant improvements for functional imaging?* [Journal of Magnetic Resonance Imaging](#) **34**, 173 (2011).
- [14] S. S. Hidalgo-Tobon, *Theory of gradient coil design methods for magnetic resonance imaging*, [Concepts in Magnetic Resonance Part A](#) **36A**, 223 (2010).

- [15] F. A. Breuer, M. Blaimer, M. F. Mueller, N. Seiberlich, R. M. Heidemann, M. A. Griswold, and P. M. Jakob, *Controlled aliasing in volumetric parallel imaging (2D CAIPIRINHA)*, [Magnetic Resonance in Medicine](#) **55**, 549 (2006).
- [16] H. Moriguchi and J. L. Duerk, *Bunched Phase Encoding (BPE): A new fast data acquisition method in MRI*, [Magnetic Resonance in Medicine](#) **55**, 633 (2006).
- [17] M. Uecker, F. Ong, J. I. Tamir, D. Bahri, P. Virtue, J. Y. Cheng, T. Zhang, and M. Lustig, *Berkeley advanced reconstruction toolbox*, in *Proc. Intl. Soc. Mag. Reson. Med*, Vol. 23 (2015).
- [18] A. SCHWARZL, *GPU Regridding of Radial 3 -D MRI data*. (2012).
- [19] D. J. Larkman, *The g-Factor and Coil Design*, [Parallel Imaging in Clinical MR Applications](#) **3**, 37 (2007).
- [20] D. Polak, S. Cauley, S. Y. Huang, M. G. Longo, J. Conklin, B. Bilgic, N. Ohringer, E. Raithel, P. Bachert, L. L. Wald, and K. Setsompop, *Highly-accelerated volumetric brain examination using optimized wave-CAIPI encoding*, [Journal of Magnetic Resonance Imaging](#) **50**, 961 (2019).
- [21] H. Wang, Z. Qiu, S. Su, S. Jia, Y. Li, X. Liu, H. Zheng, and D. Liang, *Parameter optimization framework on wave gradients of Wave-CAIPI imaging*, [Magnetic Resonance in Medicine](#) **83**, 1659 (2020).
- [22] B. E. Dietrich, D. O. Brunner, B. J. Wilm, C. Barmett, S. Gross, L. Kasper, M. Haeberlin, T. Schmid, S. J. Vannesjo, and K. P. Pruessmann, *A field camera for MR sequence monitoring and system analysis*, [Magnetic Resonance in Medicine](#) **75**, 1831 (2016).
- [23] P. M. Robson, A. K. Grant, A. J. Madhuranthakam, R. Lattanzi, D. K. Sodickson, and C. A. McKenzie, *Comprehensive quantification of signal-to-noise ratio and g-factor for image-based and k-space-based parallel imaging reconstructions*, [Magnetic Resonance in Medicine](#) **60**, 895 (2008).